First-principles Analysis of Functional Oxides and Metal Organic Frameworks

A Thesis

Submitted For the Degree of

MASTER OF SCIENCE (ENGINEERING)

in the Faculty of Science

by

Vinay Ishwar Hegde

THEORETICAL SCIENCES UNIT
JAWAHARLAL NEHRU CENTRE FOR ADVANCED SCIENTIFIC RESEARCH
Bangalore 560 064, INDIA

December 2013

to football and other untimely pursuits,

and as always, to you, Amma.

DECLARATION

I hereby declare that the matter embodied in the thesis entitled "**First-principles Analysis of Functional Oxides and Metal Organic Frameworks**" is the result of investigations carried out by me at the Theoretical Sciences Unit, Jawaharlal Nehru Centre for Advanced Scientific Research, Bangalore, India under the supervision of Prof. Umesh V. Waghmare, and that it has not been submitted elsewhere for the award of any degree or diploma.

In keeping with the general practice in reporting scientific observations, due acknowledgement has been made whenever the work described is based on the findings of other investigators.

Vinay Ishwar Hegde

CERTIFICATE

I hereby certify that the matter embodied in this thesis entitled "**First-principles Analysis of Functional Oxides and Metal Organic Frameworks**" has been carried out by Mr. Vinay Ishwar Hegde at the Theoretical Sciences Unit, Jawaharlal Nehru Centre for Advanced Scientific Research, Bangalore, India under my supervision and that it has not been submitted elsewhere for the award of any degree or diploma.

Prof. Umesh V. Waghmare

(Research Supervisor)

Acknowledgements

I would like to express my deep gratitude to Prof. Umesh Waghmare, for all the unwavering support and guidance he has given me over the past two years. He has always given me freedom regarding my work, and has taught me the right way to do science.

I would like to thank Prof. A. K. Cheetham and Dr. Jin-Chong Tan for collaborative efforts in our work on MOFs. I would like to thank Prof. C. N. R. Rao, Prof. A. Sundaresan, Mr. Rana Saha, Mr. Nitesh Kumar, Mr. Srikanth Revoju, and Ms. Urmimala Maitra for collaborations on the projects on functional oxides.

I would like to thank all my teachers here at JNCASR: Prof. Shobhana Narasimhan for making Solid State Physics (and the scientific way of writing a recipe to make tea!) so very enjoyable, Prof. Umesh Waghmare for the course on Computational Materials Science and a part of Solid State Physics, Prof. Srikanth Sastry for Monte Carlo methods, Prof. Kavita Jain for rekindling my love for math and her overflowing enthusiasm, Prof. Balasubramanian Sundaram for his FORTRAN90 classes, Prof. Chandrabhas Narayana for his classes on Group Theory, Prof. Subir Das for the several anecdotes in the Statistical Mechanics classes, Profs. Swapan Pati and Vidhyadhiraja for introducing me to quantum mechanics.

I would like to acknowledge here the support in the form of computational facilities provided by the Centre for Computational Materials Science (CCMS), JNCASR using which some of the calculations in this work were performed.

I also extend my gratitude to all the administrative and non-academic staff at JNCASR for making my stay here a very pleasant and enviable one.

My labmates, in particular, Sharmila, Meha, Anjali, Abhishek, Summayya, Jayashree, Koushik, and Krishnamohan, provided an eternal cheer and were a robust sounding board: thank you.

I thank my friends, in no particular order, Sunila, Chakri, Croor, Cindu, Shanks, Meenax, Sarada, Sona, Pripri, Ananthu, for being with me through everything. Lakumi, for being that special friend and companion.

I thank my family for supporting me through all my endeavours. I would not be here if not for them.

Sharanappa's coffee is always one cup of blissful fuel, and an inevitable, irreplaceable afternoon routine. My heartfelt thanks to him, his inconsequential banter and the life-saving caffeine.

Finally, football was my day-to-day elixir at JNC. I take this opportunity to thank the football community here for rejuvenating me every evening, letting me take my frustrations out on the field, and for all those, almost literally, battle-scars-infused memories.

List of Figures

List of Tables

Contents

Chapter 1

Introduction

> *"Is there a way of simulating it, rather than imitating it?"*
>
> - Richard Feynman, *Simulating Physics with Computers*

Our quality of life is increasingly dependent on the advances in technology, which is in turn often furthered (impeded) by the (lack of) advances in materials. During and immediately following the industrial revolution in the nineteenth century, the advances in construction and transportation were driven by the advances in procurement and production of metals and alloys. Similarly, the post Second World War era saw unprecedented advances in polymers, ceramics, superalloys, and semiconductors. The information age [1] of today is driven by speed and size. Coupled with increasing energy demands, astronomical amounts of data handling, rapid progress in the field of medicine and health care, today's materials research correspondingly focuses on efficient methods of energy storage [2], alternative fuels [3], increasing capacities of data storage and retrieval [4], effective vaccines with accurate drug delivery systems [5], and so on.

These advances in materials science and technology are primarily due to our increasingly better understanding of the processing-stucture-property relationships in materials. This is made possible by (a) state-of-the-art instruments like electron microscopes, atom probes and the like, which help us study the structure of materials at scales hitherto not possible, and (b) rapid advances in the field of computational materials science which enable us to characterize material properties which are not easily (or economically) accessible by experiments. In particular, recent advances in the field of electronic structure theory enable us to determine, without any empirical input, from the Schrödinger equation for electrons, many properties of materials. Coupled with advances in computers, this makes it possible for us to determine material behaviour and properties with an accuracy comparable to experiments, and make specific predictions for experimentally observable phenomena. This is often referred to as the first-principles theoretical approach [6]. Here, we use first-principles theory to understand experiments reporting interesting behaviour of functional oxides and metal organic frameworks.

We organize the rest of the thesis as follows: We discuss the first-principles theories and formalisms used, mainly, density functional theory (DFT) and density functional tight binding (DFTB): their theoretical basis, the practical aspects of their implementation, the approximations used, their advantages and limitations, etc., briefly in Chapter 2.

Metal organic frameworks are nanoporous materials that have found important applications in increasingly numerous applications ranging from gas storage to drug delivery. Since their mechanical stability is crucial for any industrial application, there is a need to systematically characterize their

response to mechanical stress. Recent works report a study of the complete linear elastic profile of a metal organic framework, ZIF-8, and its easy amorphization in a ball-mill. We tackle this curious observation of facile amorphization in Chapter 3.

Oxide materials have become high-tech functional materials beyond their traditional role as dielectrics. They show a rich variety of behaviour, such as impressive optical properties, catalytic activity and complex multiferroic effects. Further, they have been doped in various ways, and to various amounts, to engineer their more attractive properties. Here, heavy co-substitution with nitrogen and fluorine is seen to impart interesting electronic, optical and catalytic properties to two functional oxides, zinc oxde (Chapter 4) and titanium dioxide (Chapter 5). We study the effects of this co-substitution and its effects at the atomistic level using first-principles theory. We summarize our work and conclude in Chapter 6.

Chapter 2

Methodology and Formalisms

"Here is my lens. You know my methods."

- Sherlock Holmes, *The Adventure of the Blue Carbuncle*

The central objective of electronic structure theory is to predict a diverse array of phenomena exhibited by matter, starting from the hamiltonian for a system of nuclei and electrons [7] given by

$$\begin{aligned}\hat{H} = &-\frac{\hbar^2}{2m_e}\sum_i \nabla_i^2 - \sum_{i,I}\frac{Z_i e^2}{|\mathbf{r}_i - \mathbf{R}_I|} + \frac{1}{2}\sum_{i\neq j}\frac{e^2}{|\mathbf{r}_i - \mathbf{r}_j|} \\ &-\sum_I \frac{\hbar^2}{2M_I}\nabla_I^2 + \frac{1}{2}\sum_{I\neq J}\frac{Z_I Z_J e^2}{|\mathbf{R}_I - \mathbf{R}_J|}\end{aligned} \tag{2.1}$$

where electrons are denoted by lower case subscripts and nuclei, with charge Z_I and mass M_I, are denoted by upper case subscripts. Since the mass of the nuclei M_I are much "larger" than those of electrons m_e, the kinetic energy of nuclei in Equation 2.1 can be safely neglected in most solids. This is often referred to as the Born-Oppenheimer or adiabatic approximation. Thus, we shall focus on the hamiltonian for electrons, in which the position of the

nuclei are parameters.

The fundamental hamiltonian can now be rewritten as

$$\hat{H} = \hat{T} + \hat{V}_{ext} + \hat{V}_{ee} + E_{II} \tag{2.2}$$

where $\hat{T}$ is the kinetic energy operator for electrons,

$$\hat{T} = -\frac{\hbar^2}{2m_e} \sum_i \nabla_i^2 \tag{2.3}$$

$\hat{V}_{ext}$ is the potential acting on the electrons due to the nuclei,

$$\hat{V}_{ext} = -\sum_{i,I} \frac{Ze^2}{|\mathbf{r}_i - \mathbf{R}_I|} \tag{2.4}$$

$\hat{V}_{ee}$ is the electron-electron interaction,

$$\hat{V}_{ee} = \frac{1}{2} \sum_{i \neq j} \frac{e^2}{|\mathbf{r}_i - \mathbf{r}_j|} \tag{2.5}$$

and the final term E_{II} is the electrostatic nucleus-nucleus (or ion-ion) interaction, which is essential in the total energy calculation, but is only a classical additive term, and hence will be skipped from further discussions.

The force acting on a nucleus at $\mathbf{R}_I$ is then easily written as

$$\begin{aligned} F_I = -\frac{\partial E}{\partial R_I} &= -\langle \psi \,|\, \frac{\partial \hat{H}}{\partial \mathbf{R}_I} \,|\, \psi \rangle \\ &= -\int n(\mathbf{r}) \, \frac{\partial \hat{V}_{ext}(\mathbf{r})}{\partial \mathbf{R}_I} \, d^3r \end{aligned} \tag{2.6}$$

where the charge density $n(\mathbf{r}) = \langle\psi| \sum_i \delta(\mathbf{r} - \mathbf{r_i})|\psi\rangle$, and ψ is the many-body wavefunction. This is often referred to as the "Hellman-Feynman theorem". The procedure to obtain the aforementioned charge density for a system leads us to the foundations of the two first-principles methods we have used in this work: density functional theory (DFT) and density functional tight binding (DFTB), both of which we discuss briefly in the following sections.

We would like to mention here that the variations of ground state total energy obtained from the hamiltonian in Equation 2.1 determines several properties of materials - mechanical, electrostatic, thermal, etc. For example, the stress tensor $\sigma_{\alpha\beta}$ is given by

$$\sigma_{\alpha\beta} = -\frac{1}{\Omega}\frac{\partial E_{total}}{\partial u_{\alpha\beta}} \tag{2.7}$$

where $u_{\alpha\beta}$ is the symmetric strain tensor defined as

$$u_{\alpha\beta} = \frac{1}{2}\left(\frac{\partial u_\alpha}{\partial \mathbf{r}_\beta} + \frac{\partial u_\beta}{\partial \mathbf{r}_\alpha}\right) \tag{2.8}$$

where u_i is the displacement field as a function of the coordinate $\mathbf{r}_i$, and α and β are Cartesian indices.

Similarly, lattice vibrations are described as variations in the total energy around the equilibrium configuration with respect to second order of displacements. The force constant matrix is defined as

$$K_{IJ}^{\alpha\beta} = \frac{\partial^2 E_{tot}}{\partial \mathbf{R}_{I\alpha}\, \partial \mathbf{R}_{J\beta}} \tag{2.9}$$

where $\mathbf{R}_I$ denote nuclear coordinates, and α, β are Cartesian indices. The full

solution for all vibrational states is the set of independent oscillators, each with vibrational frequency ω determined as the eigenvalues of the dynamical matrix $\frac{K_{IJ}^{\alpha\beta}}{\sqrt{M_I M_J}}$, where M_I denotes the mass of nucleus I.

2.1 Density Functional Theory

2.1.1 Hohenberg-Kohn Theorems

The fundamental tenet of density functional theory (DFT) is that *any* property of a system of many interacting particles can be viewed as a *functional* of the ground state charge density $n_0(\mathbf{r})$. This is based upon two theorems first proved by Hohenberg and Kohn in 1964:

Theorem I: For any system of interacting particles in an external potential $V_{ext}(\mathbf{r})$ the potential $V_{ext}(\mathbf{r})$ is uniquely determined by the ground state particle density $n_0(\mathbf{r})$

Theorem II: A *universal functional* for the energy $E[n]$ in terms of the density $n(\mathbf{r})$ can be defined, valid for any external potential $V_{ext}(\mathbf{r})$. For any particular $V_{ext}(\mathbf{r})$, the exact ground state energy of the system is the global minimum value of this functional, and the density $n(\mathbf{r})$ that minimizes this functional is the exact ground state density $n_0(\mathbf{r})$.

2.1.2 The Kohn-Sham Ansatz

The challenge posed by the Hohenberg-Kohn theorems is to make use of the reformulation of many-body theory in terms of functionals of density. This leads us to the Kohn-Sham *ansatz* which assumes that the exact ground state

density of the interacting many-body system can be exactly represented by the ground state density of an auxiliary system of non-interacting particles. The density of the auxiliary system is given by the sums of squares of the N Kohn-Sham orbitals,

$$n(\mathbf{r}) = \sum_{i=1}^{N} |\psi_i(\mathbf{r})|^2 \tag{2.10}$$

the independent-particle kinetic energy T_s is given by

$$T_s = -\frac{\hbar^2}{2m_e} \sum_{i=1}^{N} \langle \psi_i | \nabla^2 | \psi_i \rangle = -\frac{\hbar^2}{2m_e} \int d^3r \, |\nabla \psi_i(\mathbf{r})|^2 \tag{2.11}$$

and the classical Coulomb interaction energy of the electron density $n(\mathbf{r})$ interacting with itself is given by

$$E_{Hartree}[n] = \frac{1}{2} \int d^3r \, d^3r' \frac{n(\mathbf{r}) \, n(\mathbf{r}')}{|\mathbf{r} - \mathbf{r}'|} \tag{2.12}$$

The Kohn-Sham approach is to rewrite the expression for the ground state energy functional (2.2) in the form

$$E_{KS} = T_s[n] + \int d\mathbf{r} \, V_{ext}(\mathbf{r}) \, n(\mathbf{r}) + E_{Hartree}[n] + E_{xc}[n] \tag{2.13}$$

Here, all the many-body effects of exchange and correlation are grouped into the exchange-correlation energy E_{xc}. Comparing the Hohenberg-Kohn (2.2) and Kohn-Sham (2.13) expressions for total energy, E_{xc} can be written in the revealing form:

$$E_{xc}[n] = \langle \hat{T} \rangle - T_s[n] + \langle \hat{V}_{ee} \rangle - E_{Hartree}[n] \tag{2.14}$$

Even though the exact functional $E_{xc}[n]$ must be very complex, great progress has been made with reasonable approximations of it being local or nearly local functional of the density.

2.1.3 The Kohn-Sham Equations

The solution of the Kohn-Sham auxiliary system for the ground state can be viewed as the problem of minimization of the total energy with respect to either the density $n(\mathbf{r})$ or the effective potential $V_{eff}(\mathbf{r})$. Thus, the variational equation is:

$$\frac{\delta E_{KS}}{\delta \psi_i(\mathbf{r})} = \frac{\delta T_S}{\delta \psi_i(\mathbf{r})} + \left[\frac{\delta E_{ext}}{\delta n(\mathbf{r})} + \frac{\delta E_{Hartree}}{\delta n(\mathbf{r})} + \frac{\delta E_{xc}}{\delta n(\mathbf{r})} \right] \frac{\delta n(\mathbf{r})}{\delta \psi_i(\mathbf{r})} = 0 \tag{2.15}$$

subject to the orthonormalization constraints

$$\left\langle \psi_i | \psi_j \right\rangle = \delta_{i,j} \tag{2.16}$$

Using the Lagrange multiplier method for handling the constraints, they lead to the Kohn-Sham Schrödinger-like equations:

$$\left(H_{KS} - \epsilon_i \right) \psi_i(\mathbf{r}) = 0 \tag{2.17}$$

where the ϵ_i are the eigenvalues, and H_{KS} is the effective hamiltonian

$$H_{KS}(\mathbf{r}) = -\frac{\hbar^2}{2m}\nabla^2 + V_{eff}(\mathbf{r}) \tag{2.18}$$

with

$$V_{eff}(\mathbf{r}) = V_{ext}(\mathbf{r}) + V_{Hartree}(\mathbf{r}) + V_{xc}(\mathbf{r}) \tag{2.19}$$

Thus, the equations have the form of independent-particle equations with a potential that must be found self-consistently with the resulting density. These equations are independent of any approximation to the functional $E_{xc}[n]$, and would lead to exact ground state density and energy if the exact functional were known. An actual calculation employs a numerical procedure [8] that successively changes V_{eff} and n to approach a self-consistent solution (see Figure 2.1).

2.1.4 The E_{xc} Functional: Approximations

We discuss in brief a few widely used approximations for the $E_{xc}[n]$ functional:

Local Density Approximation (LDA): The exchange correlation (XC) energy is simply an integral over all space with the XC energy density at each point ϵ_{xc}^{hom} assumed to be the same as in a homogeneous electron gas with that density,

$$E_{xc}^{LDA}[n] = \int d^3r \; n(\mathbf{r})\, \epsilon_{xc}^{hom}(n(\mathbf{r})) \tag{2.20}$$

Generalized Gradient Approximation (GGA): With a step beyond LDA, the XC energy density is assumed to be a functional of the magnitude

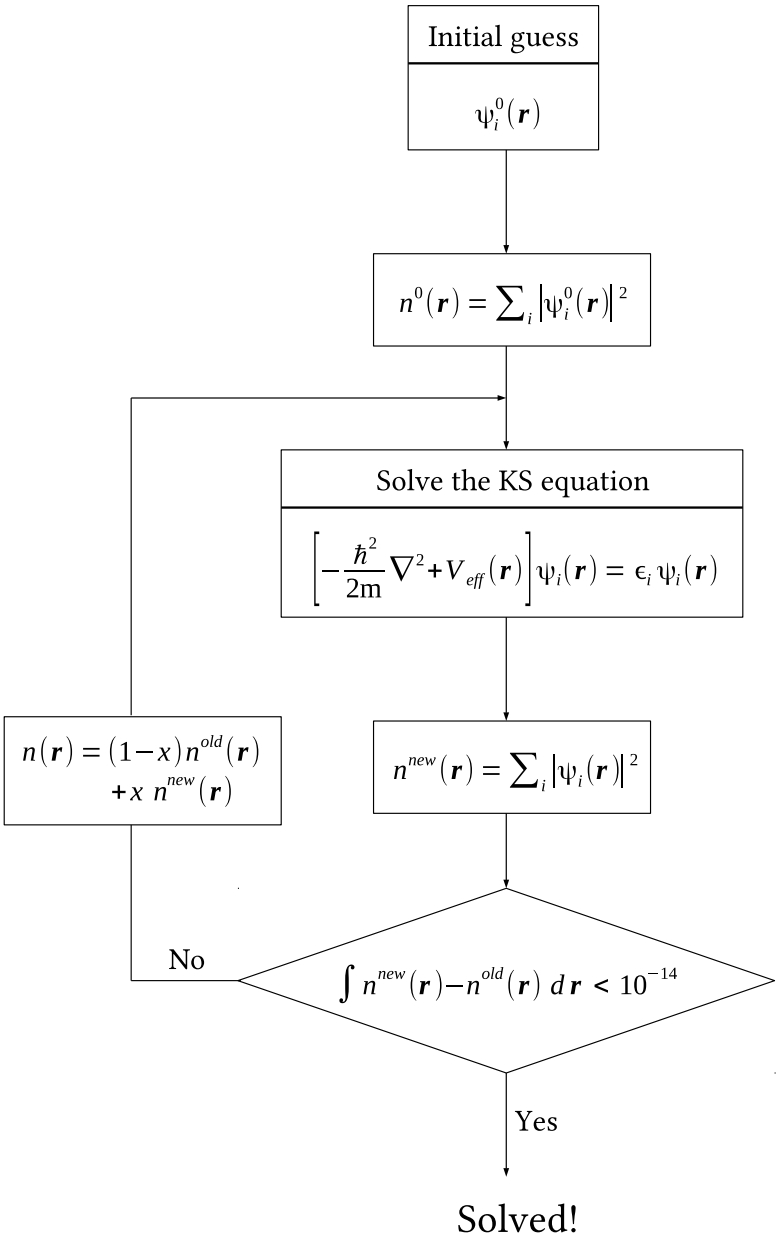

Figure 2.1: Schematic representation of the self-consistent loop for the solution of the Kohn-Sham equations (10^{-14} is just an arbitrary threshold here)

of the gradient of the density $|\nabla n|$ as well as the value of n at each point,

$$E_{xc}^{GGA}[n] = \int d^3r\, n(\mathbf{r})\epsilon_{xc}(n, |\nabla n|) \tag{2.21}$$

Typically, GGA leads to a greater lowering of the exchange energy in molecules than in solids, resulting in partial correction of the overbinding typical of LDA and thus improving agreement with experiment.

Hybrid Functionals: The XC energy functional incorporates a portion of exact exchange (in terms of the most accurate Kohn-Sham orbitals) from Hartree-Fock theory with exchange and correlation from other sources. For instance, the HSE (Heyd-Scuseria-Ernzerhof) XC energy functional uses an error function screened Coulomb potential to calculate the exchange portion of the energy in order to improve computational efficiency,

$$E_x^{HSE} = aE_x^{HF,SR}(\omega) + (1-a)E_x^{PBE,SR}(\omega) + E_x^{PBE,LR}(\omega) + E_c^{PBE} \quad (2.22)$$

where $a = \frac{1}{4}$ is the mixing parameter and ω is an adjustable parameter controlling the short-rangeness of the interaction, $E_x^{HF,SR}$ is the short range Hartree-Fock exact exchange functional, $E_x^{PBE,SR}(\omega)$ and $E_{xc}^{PBE,LR}(\omega)$ are the short and long range components of the PBE exchange functional [9], and E_c^{PBE} is the PBE correlation functional [9].

Hybrid functionals are currently the most accurate functionals available as far as calculation of properties such as band gaps is concerned but they tend to be computationally much more expensive than simple LDA and GGA calculations.

2.1.5 Other Sources of Approximation

Basis Sets

We describe two very popular approaches (used in this work) to the calculation of independent particle electronic states using the Kohn-Sham equations. Each of the approaches leads to instructive, complementary ways to understand electronic structure and can be developed into a general framework for accurate calculations.

1. Plane wave methods:

   Using the fact that any periodic function can be expanded in the complete set of Fourier components, a solution to the Kohn-Sham equations can be written as

   $$\psi_i(\mathbf{r}) = \sum_{\mathbf{q}} c_{i,\mathbf{q}} \frac{1}{\Omega} \exp(i\mathbf{q}\cdot\mathbf{r}) \equiv \sum_{\mathbf{q}} c_{i,\mathbf{q}} |\mathbf{q}\rangle \tag{2.23}$$

   where $c_{i,\mathbf{q}}$ are the expansion coefficients of the wavefunction in the basis of orthonormal plane waves $|\mathbf{q}\rangle$ satisfying

   $$\langle \mathbf{q}|\mathbf{q}'\rangle \equiv \frac{1}{\Omega}\int_{\Omega} d\mathbf{r} \exp(-i\mathbf{q}'\cdot\mathbf{r}) \exp(i\mathbf{q}\cdot\mathbf{r}) = \delta_{\mathbf{q},\mathbf{q}'} \tag{2.24}$$

   and the sum over $\mathbf{q}$ is restricted to $\mathbf{q} = \mathbf{k} + \mathbf{G_m}$ where $\mathbf{k}$ is a general wave vector and $\mathbf{G_m}$ are the reciprocal lattice vectors.

   Generally, for calculation of properties like total energy by integrating over $\mathbf{k}$ throughout the Brillouin zone (BZ), only planewaves with kinetic energy less than a certain threshold ($\frac{1}{2}|\mathbf{k}+\mathbf{G}|^2 < E_{cutoff}$) are used

to represent wavefunctions. To minimize errors from this source of approximation, it is a good practice to use a cutoff energy after studying the convergence behaviour of total energy with respect to the aforesaid cutoff E_{cutoff}.

There are several planewave-based total energy codes that are widely used today: QUANTUM ESPRESSO, VASP, ABINIT, CASTEP among others.

2. Linear Combination of Atomic(-like) Orbitals (LCAO):

   Here, the eigensolutions to the Kohn-Sham equations are written in the form

$$\psi_{i,\mathbf{k}}(\mathbf{r}) = \sum_{p} c_p(\mathbf{k}) \chi_{p,\mathbf{k}}(\mathbf{r}) \tag{2.25}$$

   where $\chi_\alpha(\mathbf{r})$ is a basis set of atomic-like orbitals centered on the atom sites, written as radial functions multiplied by spherical harmonics as follows

$$\chi_\alpha(\mathbf{r}) \rightarrow \chi_{nlm}(\mathbf{r}) = \chi_{nl}(r)\, Y_{lm}(\hat{\mathbf{r}}) \tag{2.26}$$

   where n indicates different functions with the same angular momentum, and $p = 1, \ldots, N_{basis}$ labels all the states in the basis.

   As of now, there is a lack of a systematic recipe for optimizing the size and type of basis sets used and this can lead to small errors creeping into total energy calculations. There are several popular LCAO codes in use today: SIESTA, ATK, PLATO, among others.

Pseudopotentials

Since valence wavefunctions tend to have rapid oscillations near ion cores due to the requirement that they be orthogonal to core states, a huge number of Fourier components (or in the case of grid-based methods, a very fine mesh) are required to describe the wavefunctions accurately. The pseudopotential is an effective potential constructed to replace the atomic all-electron potential (full-potential) such that core states are eliminated and the valence electrons are described by nodeless pseudo-wavefunctions (see Figure 2.2). In this approach only the chemically active valence electrons are dealt with explicitly, while the core electrons are 'frozen', being considered together with the nuclei as rigid non-polarizable ion cores. Pseudopotentials with larger cutoff radius are said to be 'softer', that is more rapidly convergent, but at the same time less transferable, that is less accurate to reproduce realistic features in different environments. While the small core approximation assumes that there is no significant overlap between core and valence wavefunctions, non-linear core correction methods and the inclusion of semi-core electrons deal with situations where the overlap is non-negligible. Thus, the main motivation is the reduction in the number of electrons (thus, decreased computational costs) and the possibility of the inclusion of relativistic and other effects.

Norm-conserving pseudopotentials enforce the condition that, outside of a cutoff radius (r_c), the norm of each pseudo-wavefunction be identical to its corresponding all-electron wavefunction. Ultrasoft pseudopotentials generalize the norm-conserving constraint to reduce the basis-set size further, resulting a greater reduction in computational costs.

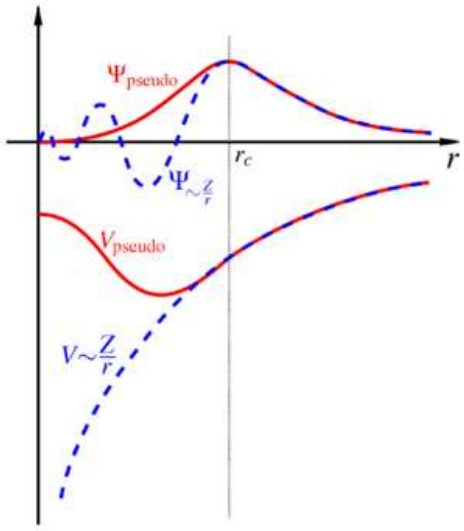

Figure 2.2: Comparison of a wavefunction in the Coulomb potential of the nucleus (blue) to the one in the pseudopotential (red). The real and the pseudo wavefunction and potentials match above a certain cutoff radius r_c. (Image source: Wikipedia)

2.2 Density Functional Tight Binding

2.2.1 Formalism

The self-consistent charge density functional tight binding (SCC-DFTB or simply DFTB) method is based on a second order expansion of the Kohn-Sham total energy in DFT with respect to charge density fluctuations [10]. Recalling that the Kohn-Sham total energy of a system of M electrons in the field of N nuclei at positions $\mathbf{R}$ can be written as a functional of charge

density $n(\mathbf{r})$ as

$$E = \sum_i \left\langle \psi_i \right| - \frac{\hbar^2}{2m_e}\nabla^2 + V_{ext} + \frac{1}{2}\int \frac{n(\mathbf{r}')}{|\mathbf{r}-\mathbf{r}'|} dr' \left| \psi_i \right\rangle + E_{xc}[n(\mathbf{r})] + \frac{1}{2}\sum_{\alpha,\beta}^{N} \frac{Z_\alpha Z_\beta}{|\mathbf{R}_\alpha - \mathbf{R}_\beta|} \tag{2.27}$$

where the first sum is over occupied Kohn-Sham eigenstates ψ_i, the second term is the exchange-correlation (XC) contribution, and the last term is the ion-ion core repulsion, E_{II}. The charge density in Equation (2.27) is now substituted by a superposition of a reference or input density $n_0' = n_0(\mathbf{r}')$ and a small fluctuation $\delta n' = \delta n'(\mathbf{r}')$:

$$\begin{aligned} E = &\sum_i \left\langle \psi_i \right| - \frac{\hbar^2}{2m_e}\nabla^2 + V_{ext} + \int \frac{n_0'}{|\mathbf{r}-\mathbf{r}'|} dr' + V_{xc}[n_0] \left| \psi_i \right\rangle \\ &- \frac{1}{2}\int\int \frac{n_0'\,(n_0+\delta n)}{|\mathbf{r}-\mathbf{r}'|} dr\, dr' - \int V_{xc}[n_0](n_0+\delta n) dr \\ &+ \frac{1}{2}\int\int \frac{\delta n'(n_0+\delta n)}{|\mathbf{r}-\mathbf{r}'|} dr\, dr' + E_{xc}[n_0+\delta n] + E_{II} \end{aligned} \tag{2.28}$$

The second term in this equation corrects for the double counting of the Hartree term, the third term for the new XC contribution in the leading matrix element, and the fourth term results from dividing the full Hartree energy in Equation (2.27) into a part related to n_0 and to one δn. Expanding E_{xc} at the reference density, total energy correct to second order in density

fluctuations is obtained:

$$E = \sum_i \left\langle \psi_i \middle| \hat{H}_0 \middle| \psi_i \right\rangle - \frac{1}{2} \int\int \frac{n_0' \, n_0}{|\mathbf{r} - \mathbf{r}'|} dr \, dr' + E_{xc}[n_0] \\ - \int V_{xc}[n_0] n_0 dr + E_{II} + \frac{1}{2} \int\int \left(\frac{1}{|\mathbf{r} - \mathbf{r}'|} + \left. \frac{\delta^2 E_{xc}}{\delta n \; \delta n'} \right|_{n_0} \right) \delta n \, \delta n' \quad (2.29)$$

where $\hat{H}_0$ is the hamiltonian operator representing the first term in Equation (2.28).

The charge fluctuation is now decomposed into atom centered contributions which decay fast with increasing distance from the corresponding center (expanded in a series of radial and angular functions):

$$\delta n_\alpha(\mathbf{r}) = \sum_{l,m} K_{ml} F^\alpha_{ml}(|\mathbf{r} - \mathbf{R}_\alpha|) Y_{lm} \left(\frac{\mathbf{r} - \mathbf{R}_\alpha}{|\mathbf{r} - \mathbf{R}_\alpha|} \right) \\ \approx \Delta q_\alpha F^\alpha_{00}(|\mathbf{r} - \mathbf{R}_\alpha|) Y_{00} \quad (2.30)$$

where F^α_{ml} denotes the normalized radial dependence of the density fluctuations on atom α for the corresponding angular momentum, and Δq_α are charge fluctuations. Thus the second order term in Equation (2.29) now has the form

$$E_2 = \frac{1}{2} \sum_{\alpha,\beta}^{N} \int\int \Gamma[\mathbf{r}, \mathbf{r}', n_0] \; \delta n_\alpha(\mathbf{r}) \, \delta n_\beta(\mathbf{r}') dr \, dr' \quad (2.31)$$

where the functional Γ denotes the Hartree and XC coefficients (from Equation 2.29). Since Equation (2.31) preserves the total charge in the system,

i.e., $\sum_\alpha \Delta q_\alpha = \int \delta n(\mathbf{r}) dr$, the second order term can simply be written as

$$E_2 = \frac{1}{2} \sum_{\alpha,\beta}^{N} \Delta q_\alpha \Delta q_\beta \gamma_{\alpha\beta} \tag{2.32}$$

where

$$\gamma_{\alpha\beta} = \int\int \Gamma[\mathbf{r}, \mathbf{r}', n_0] \frac{F_{00}^{\alpha}(|\mathbf{r} - \mathbf{R}_\alpha|) F_{00}^{\beta}(|\mathbf{r} - \mathbf{R}_\beta|)}{4\pi} \, dr \, dr' \tag{2.33}$$

Thus, the total energy can be written as

$$E^{DFTB} = \sum_i \left\langle \psi_i \middle| \hat{H}_0 \middle| \psi_i \right\rangle + \frac{1}{2} \sum_{\alpha,\beta}^{N} \gamma_{\alpha,\beta} \Delta q_\alpha \Delta q_\beta + E_{II} \tag{2.34}$$

2.2.2 Solving the DFTB Kohn-Sham Equation

To solve the DFTB Kohn-Sham equation (2.34), the single-particle wavefunctions ψ_i are expanded into a suitable set of localized Slater-like atomic orbitals ϕ_ν (assuming an exponential decay of the normalized spherical charge densities $n_\alpha(r) \sim e^{-|\mathbf{r}-\mathbf{R}_\alpha|}$), and the charge fluctuations are estimated using Mulliken charge analysis. By applying the variational principle to the energy functional in Equation (2.34), the charge density is obtained in a self-consistent way.

There are several popular implementations of the DFTB method in use: DFTB+, Amber, ATK, Gaussian, among others.

2.2.3 Parameter Files

The DFTB parameters used in the calculations consist of two parts:

1. Electronic part:

   It contains atomic and diatomic contributions which are both calculated from DFT-based calculations, using either LDA or GGA functionals.

   - The atomic parameters are atomic s, p, d, ... Kohn-Sham eigenenergies, which enter as diagonal elements in the Hamiltonian.
   - The non-diagonal matrix (overlap matrix S and the Hamiltonian $\hat{H}$) elements are calculated in a two-center approximation for a neutral atomic reference density. They are distance dependent and are stored as a table for interatomic distances up to $\sim$10 a.u.

   Using these parameters, the DFTB program does not have to perform any integral evaluation during the program runtime. This reduces the computational costs significantly over conventional DFT pseudopotential codes (an improvement of the order of 10-100 is typical).

2. Repulsive part:

   The repulsive energy contribution (final term in Equation (2.27)) is approximated as a sum of pair potentials of the form $\sum_k \sum_{<l} V_{rep}(\mathbf{R}_l - \mathbf{R}_k)$, which are represented either by spline functions or by polynomials. They are derived by calculating bond stretching energies of selected bonds in a small set of molecules using DFT-based calculations.

Clearly, the parameters are optimized for specific environments and they are not as transferable as ab-initio pseudopotentials employed by standard DFT implementations. Thus, though the method provides an improvement in speed upto two orders of magnitude with respect to conventional DFT-based methods, parameter files for only a few systems, and optimized for a few environments are available as of now limiting the wide utilization of this method.

Chapter 3

Stacking Faults and Mechanical Behaviour Beyond the Elastic Limit of a Metal Organic Framework: ZIF-8*

"How often have I said to you that when you have eliminated the impossible, whatever remains, however improbable, must be the truth?"

- Sherlock Holmes, *The Sign of the Four*

3.1 Introduction

Metal organic frameworks (MOFs) are crystalline materials consisting of metal ions or clusters coordinated to organic moeities to form one-, two-, or three-dimensional porous structures. A diverse range of pore geometries and chemical functionalities have enabled MOFs to find increasing number of applications in gas storage [11], gas separation [12], catalysis [13], luminescence [14], optoelectronics [15] and drug delivery [16]. Zeolitic imidazolate

*Reproduced in part with permission from *The Journal of Physical Chemistry Letters*, submitted for publication. Unpublished work copyright 2013 *American Chemical Society*.

frameworks (ZIFs) are a sub-family of MOFs that are topologically isomorphic with inorganic zeolites. ZIFs are composed of tetrahedrally-coordinated transition metal ions (e.g. Fe, Co, Cu, Zn) connected by organic imidazole linkers. Since the metal-imidazole-metal (m-Im-m) angle is similar to the 145° Si-O-Si angle in zeolites, ZIFs take up zeolite-like topologies. ZIFs combine the pore-size tunability of MOFs and the thermal stability of zeolites, and are particularly attractive candidates for the several applications listed above. Since their mechanical stability is crucial for any technological application [17], understanding their mechanical behaviour assumes singular importance.

ZIF-8 ($Zn(mIm)_2$; mIm = 2-methylimidazolate) with the sodalite (SOD) topology, crystallizes in the cubic space group $I\bar{4}3m$ (see Figure 3.1a) with a lattice constant of 16.992 Å [18], and contains 276 atoms in the unit cell ($Zn_{12}\,N_{48}\,C_{96}\,H_{120}$). It exhibits an exceptionally large pore volume, with a solvent accessible volume (SAV) of ∼50% [19]. Recently, Tan et al. [20] studied the complete *linear* elastic response of ZIF-8 and reported an extremely low shear modulus of 0.97 GPa. This result suggested easy mechanical failure of ZIF-8 on the application of shear stresses, which was later confirmed by Cao et al. [21] who reported its rapid amorphization upon ball milling. This work explores the *nonlinear* shear and cleavage response of ZIF-8 to identify a possible mechanism of its amorphization during ball milling.

We study the nonlinear response of ZIF-8 with respect to two crystallographic modes of failure: cleavage and shear. The former occurs as a result of tensile stresses acting normal to a crystallographic cleavage plane, for which the energy rate necessary is twice the surface energy, as per the

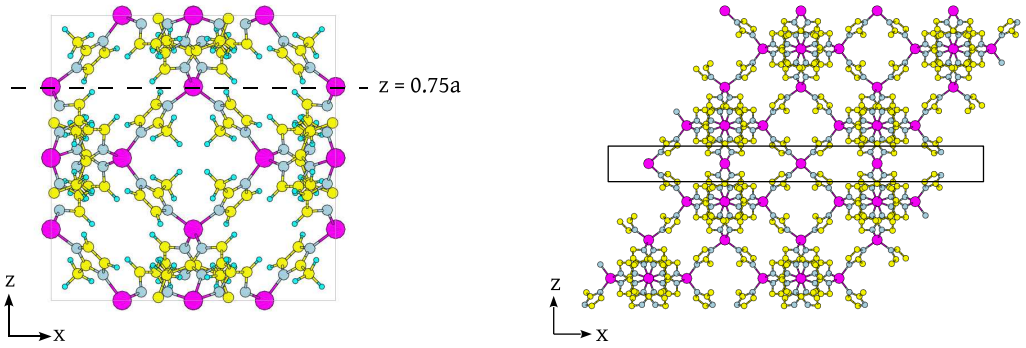

(a) (b)

Figure 3.1: (a) Unit cell of ZIF-8; (b) ISF structure with a slip vector (x, y) = (0.50, 0.50), with one SF per unit cell. The stacking fault has been enclosed by a box. It has 2 unit cells each in the x, y and z directions for better visualization. Zinc atoms are shown in pink, nitrogen atoms in blue, carbon atoms in yellow and hydrogen atoms in cyan. Hydrogen atoms have been omitted for clarity in (b).

Griffith criterion [22]. The latter occurs under the influence of shear stresses acting in-plane, resulting in extensive slip of dislocations and the formation of stacking faults, the energetics of which are captured in the generalized stacking fault energy (GSF) surface or the γ-surface [23].

3.2 Computational Methods

We have used a combination of two first-principles methods in our investigation: (a) density functional theory (DFT) as implemented in the Vienna Ab-initio Simulation Package (VASP) [24] and (b) density functional tight binding (DFTB) method as implemented in DFTB+ [25]. In the DFT-based calculations, ion-electron interactions were modelled using ultrasoft pseudopotentials [26] and the exchange-correlation functional was approximated by a generalized gradient approximation (GGA) as parameterised by Perdew

and Wang (1991) [27]. Since the DFT-based calculations were computationally very expensive, DFTB-based calculations were used for simulating the system on a larger scale. Slater-Koster files from the parameter set *znorg-0-1* [28] were used to parameterize the interactions between the elements in the system. DFTB has been successfully used to calculate the structural properties of metal organic frameworks previously [29], and we further benchmarked its parameters through comparison of its results for the stacking fault energy (SFE) with those by DFT (within 5%). Van der Waals interactions were included with a Lennard-Jones dispersion model as in DFTB+ [30], with parameters for the potential taken from the Universal Force Field (UFF) [31]. We checked the convergence of total energy with respect to the fineness of the k-mesh used, and observed that a 1×1×1 mesh was sufficiently accurate (within 0.1 meV/ unit cell) for our calculations. The positions of the atoms in the periodic cell were relaxed, keeping the lattice constant fixed at the experimental value, by minimizing the energy until Hellman-Feynman forces were within 0.002 Ry/Å. The Hessian matrix was evaluated numerically using a method of finite differences with a symmetric finite differences formula on Hellman-Feynman forces, and atomic displacements of ±0.01 Å.

We focus on stacking faults (SFs) generated on the (001) plane in ZIF-8 with a transformation of the unit cell vector:

$$\vec{c} = \vec{c}_o + x\,\vec{a} + y\,\vec{b} \tag{3.1}$$

where $\vec{a}$, $\vec{b}$ and $\vec{c}$ are the unit cell vectors. One such generated stacking fault, with slip vector $(0.5, 0.5)a$ is shown in Figure 3.1b. The corresponding SFEs

were obtained by calculating the difference between the energy of the faulted and ideal structures. The stacking fault energy as a function of x and y defines the γ-surface: $Z = E(x, y)$. Due to complexity of the hierarchical structure, not all (001) planes in ZIF-8 are equivalent, in contrast to simple metals whose crystal structures have only one or two atoms per unit cell. We choose a z-plane across which the fewest number of bonds are affected by a stacking fault, i.e. at $z = 0.75a$.

We use a uniform 4×4 mesh in the real-space planar (the (001) plane) unit cell to interpolate the data to construct a γ-surface. We have checked the numerical values obtained from the interpolation formula for the underlying symmetry and sufficient accuracy. Specifically, we use the following expression:

$$\gamma(x, y) = 0.2 \sum_{m=1}^{5} \sum_{n=1}^{5} A_{m,n}\ exp\Big\{ i(2\pi k_m x + 2\pi k_n y) \Big\} \tag{3.2}$$

where $k = \{0, 1, 2, -2, -1\}$, and $A_{m,n}$ are coefficients obtained from a discrete Fourier transform of the stacking fault energies ($\mathrm{SFE}_{m,n}$) calculated on the 4×4 spatial mesh. The coefficients $A_{m,n}$ bear the symmetry of the crystal.

3.3 Results

3.3.1 Stacking Fault Energies: γ-surface

Stacking fault energies calculated as detailed in the previous section (see Table 3.1) are interpolated according to Equation 3.2 to generate a γ-surface. A minimum of the γ-surface represents the intrinsic stacking fault energy

(γ_{isf}) of a material. For ZIF-8, it occurs at a shift (see Figure 3.2) of (0.50, 0.50)a (this structure is referred to henceforth as the 'ISF structure') with a very low γ_{isf} (~66 mJ/m^2) comparable to that of metals like copper and gold [32], and covalently bonded Si [33]. This implies that the stacking faults in ZIF-8, if present, should be wide and visible through transmission electron microscopy. In practice though, templating effect by the solvent molecules may hinder the formation of such faults, and they may not occur as commonly as expected from the energetics.

x	y	Fault Energy (mJ/m^2)
0.00	0.00	0.0
0.25	0.00	479.5
0.25	0.25	434.1
0.50	0.00	491.7
0.50	0.25	458.1
0.50	0.50	65.9

Table 3.1: Stacking fault energies obtained from DFT-based calculations.

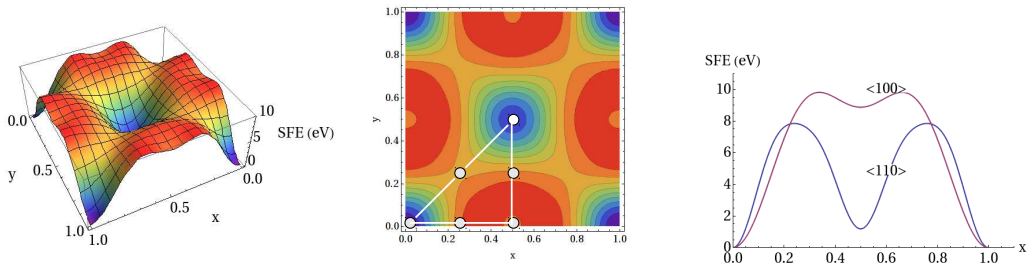

(a) (b) (c)

Figure 3.2: (a) γ-surface for the {100} plane in ZIF-8. (b) Contour plot of the γ-surface for the {100} plane in ZIF-8 showing data points used for Fourier interpolation. (c) Sections of the γ-surface along $\langle 100 \rangle$ and $\langle 110 \rangle$.

A possible dissociation reaction of the dislocation with Burgers vector $a_o\langle 110\rangle$, on the (001) plane, is

$$a_o\langle 110\rangle = \frac{a_o}{2}\langle 110\rangle + \text{SF} + \frac{a_o}{2}\langle 110\rangle$$

which results in two collinear partials and an intrinsic stacking fault.

The unstable stacking energy (γ_{usf}) of a material is defined as the lowest energy barrier to be crossed to go from the ideal structure to the ISF structure. For ZIF-8, the barrier occurs at a shift of (0.25, 0.25)a (the structure with the corresponding SF is referred to henceforth as the 'USF structure') with an estimated energy of $\sim$434 mJ/m^2. This is around 3-4 times higher than that of metals like copper and gold [34], and around 4-5 times lower than that of covalently bonded materials like Si [33].

3.3.2 Reliability Checks

To further verify the reliability of our findings, we calculated the energies of lower density stacking faults (i.e., one stacking fault per two unit cells) (Table 3.2). It can be seen that the energy cost of introducing a stacking fault per two unit cells is within 4% of that for one fault per unit cell which leads us to conclude that interaction between stacking faults in ZIF-8 is weak. This result also suggests that the properties of stacking faults in ZIF-8 are essentially dependent only on the local framework structure. Interestingly, inclusion or exclusion of van der Waals (vdW) interactions using DFTB (Table 3.2) yielded no notable changes in the SFEs.

Method	**1 SF/ unit cell** Fault Energy (mJ/m^2)	**1 SF/ 2 unit cells** Fault Energy (mJ/m^2)
DFT	65.87	63.43
DFTB	69.42	67.87
DFTB+vdW	70.92	67.92

Table 3.2: Comparison of SFE calculated using DFT, DFTB, and DFTB+vdW based calculations, for 1 SF per unit cell and 1 SF per 2 unit cells.

3.3.3 Effect on Properties and Applications

The relaxed ISF structure (Figure 3.1b) reveals that the local atomic structure does not change upon introduction of SFs and this conservation of local order suggests a low SFE, which is indeed consistent with our calculations in Table 3.1. We note that only Zn-N bonds get affected by shear or cleavage across the (001) plane at $z = 0.75a$, and these get re-formed in the ISF configuration. A comparison of electronic density of states (DoS) for the ideal and ISF structures (Figure 3.3) reveals no *conspicuous* differences, particularly across the gap. By projecting the total density of electronic states onto atomic orbitals, we find that (i) the valence band is composed almost entirely of C-2p orbitals while Zn-3d states are deep lying in energy ($\sim$4.5 eV lower than the valence band maximum), (ii) the conduction band has equal contributions from C-2p and N-2p orbitals, and (iii) these remain unaffected on the introduction of SFs. Since valence and conduction states interact effectively with a guest moiety, it is expected that gas adsorption, catalysis and other related properties of ZIF-8 will remain largely unaffected by stacking faults.

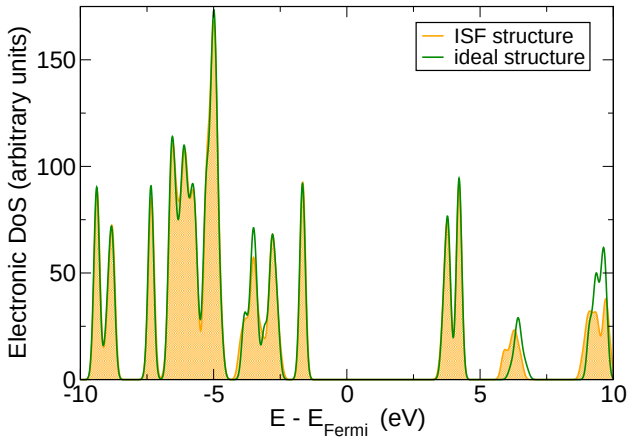

Figure 3.3: Comparison of total density of electronic states of the ideal and ISF structures

3.3.4 Vibrational Signature of the SFs

The Hessian of total energy obtained from DFTB calculations was used to determine vibrational frequencies and modes of ZIF-8. A comparison of the vibrational density of states of the ideal and ISF structures (Figure 3.4) shows the splitting of a group of modes at ∼1280 cm^{-1} into two separate groups of modes at ∼1260 cm^{-1} and ∼1230 cm^{-1}, which should constitute a Raman signature of the SFs. These modes correspond to stretching of the imidazole ring along the Zn-Im-Zn axis or perpendicular to it. Upon introduction of a fault, the imidazole rings away from the fault participate in the modes at ∼1260 cm^{-1} while those closest to the fault participate in the modes at ∼1230 cm^{-1}, indicating that chemical bonds in the imidazolate rings near the fault weaken.

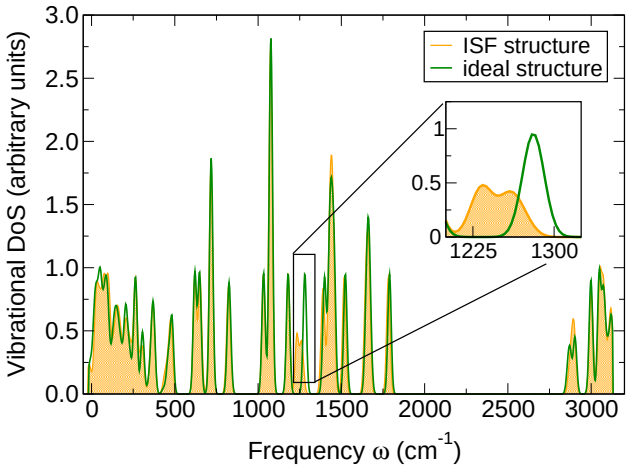

Figure 3.4: Comparison of total density of vibrational states of the ideal and ISF structures

3.3.5 Surface Energy

Although such faults have been observed in covalent-organic frameworks (COFs) [35], they are yet to be reported in ZIFs. This suggests that such faults may not be common in ZIF-8 and alternative modes of failure may be more favorable. Thus, we calculated the energy relevant to tensile mode of failure, the surface energy (γ_s), which is defined as the difference between the total energy of the bulk and that of the crystal cleaved across the required plane (here, (001) with $z = 0.75a$). Our estimate of γ_s for ZIF-8 is $\sim$280 mJ/m^2, around 5-6 times lower than that of soft, ductile metals like copper ($\sim$1.73 J/m^2) and gold ($\sim$1.48 J/m^2) [34], both of which are cubic close-packed and that of covalently bonded solids like Si ($\sim$1.36 J/m^2) [33], which has diamond cubic structure.

The ratio of surface energy to unstable stacking fault energy characterizes the brittle versus ductile tendency of a material, and is termed the 'disembrittlement parameter' ($D = \gamma_s/\gamma_{usf}$) [36]. For example, the values of D for ductile metals copper and gold are ~ 10.68 and ~ 11.5, while that for a brittle material like silicon is ~ 0.68. On this basis, our estimate of D for ZIF-8 is 0.64, which means that it is brittle, i.e. it is easier to cleave than to nucleate a dislocation necessary for plastic deformation (note that $D_{ZIF-8} \equiv D_{Si} << D_{Cu}, D_{Au}$). This preferential brittle failure may prevent the stacking faults from occurring in ZIF-8, in spite of the low γ_{isf}. This result is consistent with experimental observations in which the single crystals of hybrid frameworks are indeed susceptible to material failure by cracking, and thereby exhibit a low fracture toughness [17].

3.3.6 γ-surface and Amorphization of ZIF-8

The lack of experimental evidence for stacking faults in experiments reported so far also suggests that alternative structures more favorable than the ones with faults may exist. To investigate this possibility, we determined the vibrational spectrum of the state corresponding to the energy barrier (USF structure) that ZIF-8 must pass through to develop a fault, to analyze its local structural stability. An inspection of the vibrational density of states of the USF structure reveals structural instabilities through imaginary frequencies (see Figure 3.5a). Secondly, the USF state also exhibits a compressive stress. The presence of a compressive stress state on the structure prompted

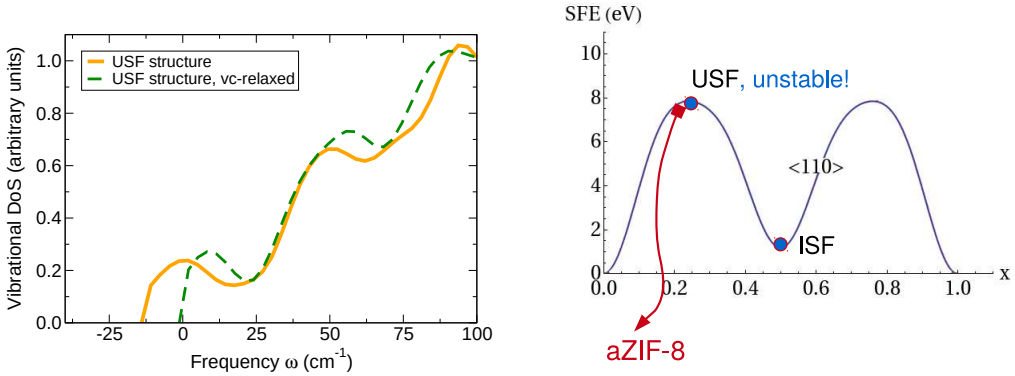

(a) (b)

Figure 3.5: (a) Comparison of vibrational density of states of the USF structure, before and after variable-cell optimization ('vc-relaxed'), revealing local instabilities; (b) Alternate energy pathway from the USF structure to amorphous ZIF-8 (aZIF-8)

us to perform variable-cell (complete) relaxation which resulted in a reduction of the cell volume by ∼10% (or a corresponding increase in the density by ∼11%). We expect similar structural instabilities arising during slips on other symmetry equivalent planes of the {100} family in the USF structure, i.e. the (100) and (010) planes (along with those on the (001) plane studied here) to lead to further reduction in the cell volume (or correspondingly, further increase in the density). As seen earlier, the energy barriers during slip to the faulted structure are quite high. Since there is no high-density crystalline phase ZIF-zni associated with ZIF-8 [37], the structural instabilities and the associated compressive stress state transform the barrier (transition) state into a lower energy disordered structure of higher density, providing an alternate pathway to the amorphous phase aZIF-8 (see Figure 3.5b). In this connection, we note that a recent calorimetric study has shown that the amorphous state is only 4.5 kJ mol^{-1} less stable than the denser phase for

ZIFs containing unsubstituted imidazole ligands [38].

3.4 Summary

We have studied the nonlinear mechanical behaviour of a prototypical imidazole-based MOF, ZIF-8, by simulating uniaxial tensile and shear modes of failure. We expect ZIF-8 to be intrinsically brittle because it is easier to cleave than to nucleate a dislocation that would enable plastic flow. A very low intrinsic stacking fault energy, comparable to copper and gold, leads us to expect the SFs in ZIF-8 to be wide, if present. We find that stacking faults do *not* alter the local atomic structure or the electronic structure of ZIF-8, and therefore are not detrimental to its physicochemical properties, auguring well for its practical applications. We identify a Raman signature of the SFs, characterized by the splitting of a peak at $\sim$1280 cm^{-1} into two distinct peaks at $\sim$1260 cm^{-1} and $\sim$1230 cm^{-1}. The lack of evidence for such faults in experiments is explained through the preferential formation of a high density amorphous phase through the release of shear and compressive stresses acting on the transition state or the barrier for the formation of a fault.

Chapter 4

Structure, Electronic and Optical Properties of ZnO Heavily Co-substituted with Nitrogen and Fluorine*

"The wind waved his hair against the sky. His hair was neither blond nor red, but the exact colour of ripe orange rind."

- Ayn Rand, *The Fountainhead*

4.1 Introduction

Zinc oxide is a ubiquitous functional oxide having found its way into numerous applications ranging from rubber manufacturing, ceramic and concrete industry to medicine, cosmetics and electronics. It is an n-type semiconductor with a direct band gap of 3.37 eV and a high concentration of native

*Reproduced in part with permission from Saha, R., Revoju, S., Hegde, V. I., Waghmare, U. V., Sundaresan, A. & Rao, C. N. R. **2013**, Remarkable Properties of ZnO Heavily Substituted with Nitrogen and Fluorine, $ZnO_{1-x}(N,F)_x$, DOI: 10.1002/cphc.201300305. Copyright 2013 WILEY-VCH Verlag GmbH & Co. KGaA

defects such as oxygen vacancies and zinc interstitials [39]. In an effort to modify its electronic properties, ZnO has been doped with other elements. While cationic substitution has been widely studied [40], anionic substitution, with high concentration of dopants in particular, has not been fully explored. Towards this end, Prof. C. N. R. Rao's group here[†] synthesized ZnO heavily co-substituted with nitrogen and fluorine ($ZnO_{1-x}(N,F)_x$), and observed a bright orange colouration associated with a reduced band gap (see Figure 4.1a), and an increased dielectric constant. We develop understanding of the effect of this co-substitution on the electronic and optical properties of ZnO at the atomistic level.

Zinc oxide naturally occurs primarily in two forms: hexagonal wurtzite and cubic zincblende. The wurtzite polymorph (studied here) is the most stable at ambient conditions and thus more common. It crystallizes in a HCP lattice (space group 186 or $P6_3mc$) with two formula units in the conventional unit cell (see Figure 4.1b), and with lattice constants $a = 3.2495$ Å, $c = 5.2069$ Å [40]. The atomic basis is given by

$$\text{Zn: } \left\{\left(\tfrac{1}{3}, \tfrac{2}{3}, 0\right), \left(\tfrac{2}{3}, \tfrac{1}{3}, \tfrac{1}{2}\right)\right\}$$
$$\text{O: } \left\{\left(\tfrac{1}{3}, \tfrac{2}{3}, u\right), \left(\tfrac{2}{3}, \tfrac{1}{3}, \tfrac{1}{2}+u\right)\right\},\ u = 0.3821$$

4.2 Computational Details

Our first-principles calculations are based on density functional theory (DFT) as implemented in SIESTA [41], QUANTUM ESPRESSO [42], and ABINIT

[†]International Centre for Materials Science, Jawaharlal Nehru Centre for Advanced Scientific Research

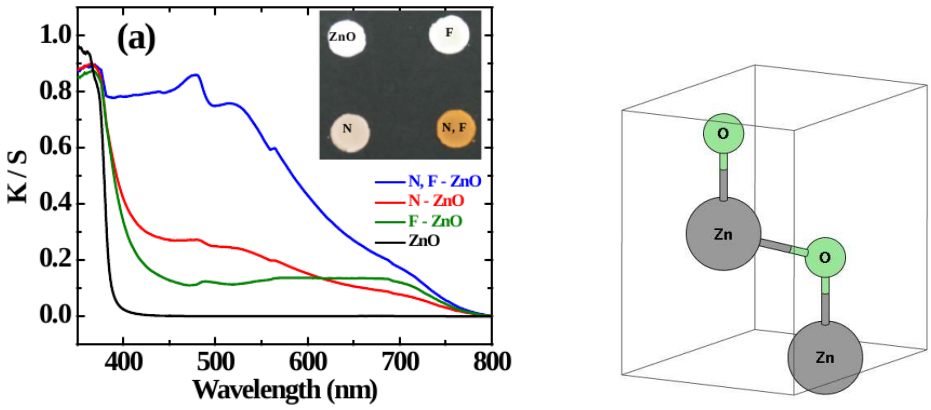

(a) (b)

Figure 4.1: (a) UV/Visible spectra of ZnO and anion-substituted ZnO; inset shows the colour of the samples in visible light, (b) Conventional unit cell of wurtzite ZnO with two formula units (Image (a): courtesy Prof. C. N. R. Rao's group, ICMS, JNCASR)

[43] These sets of calculations were used to benchmark them against each other. Subsequently, computationally intensive calculations of phonons were carried out with ESPRESSO and SIESTA and self-energy corrected estimation of the energy gap in the electronic spectrum was carried out with ABINIT using GW-approximation [44]. To model the ion-electron interactions, Troullier-Martin [45] pseudopotentials were used in SIESTA and ABINIT-based calculations, and ultrasoft pseudopotentials [26] were used in Quantum ESPRESSO-based calculations. The exchange-correlation energy functional was approximated with a local density approximation (LDA) of the Ceperly-Alder [46] form. In SIESTA-based calculations, atomic orbitals of multiple-zeta kind with a split valence scheme were used as the basis with a split norm of 0.15 and orbital-confining cutoff radii defined by an energy shift of 0.007 Ry. A kinetic energy cutoff of 50 Ry for wavefunctions and 400 Ry for charge density were used in ESPRESSO-based calculations,

and a cutoff of 80 Ry was used in the representation of wavefunctions in the self-energy corrected calculations with ABINIT.

To simulate substitutional doping at the levels achieved in experiments here, we used a 2×2×1 periodic supercell with 16 atoms by substituting (i) 1 of the O atoms by a nitrogen atom (12.5% N) for N-ZnO, (ii) 1 of the O atoms by a fluorine atom (12.5% F) for F-ZnO, and (iii) 3 of the 8 O atoms with 2 N and 1 F (25% N, 12.5% F) for N,F-ZnO. In case (iii), we exhaustively studied all the configurations of chemical ordering of F and N in the supercell. Using the symmetries of the lattice, we reduced these to 8 independent configurations (see Figure 4.2), using Site Occupancy Disorder (SOD) technique [47]. A 12×12×15 uniform grid of k-points was used to sample integrations over the Brillouin-zone of the supercell. Structures of all the configurations were relaxed till the Hellman-Feynman forces on all the atoms were 0.01 eV/Å or less, and the stresses were within 1 kbar.

4.3 Results and Discussion

4.3.1 Lattice parameters and Chemical Ordering

Our calculated lattice parameters for bulk ZnO (a = 3.2204 Å, c = 5.1875 Å) are within the LDA errors and in good agreement with the experimental and published theoretical values [48]. The change in lattice parameters on substitution of N and F at oxygen sites is within 1% of those calculated for bulk ZnO. Our analysis of the energetics of F-ZnO, N-ZnO, and N,F-ZnO

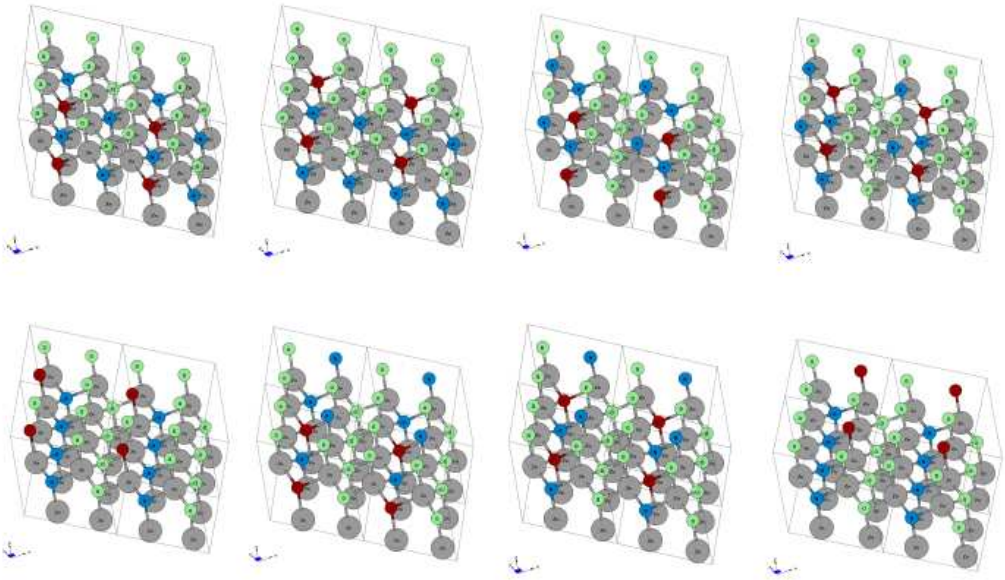

Figure 4.2: 8 independent configurations of chemical ordering of F and N in the 2×2×1 supercell (Zn atoms are shown in grey, oxygen atoms in green, nitrogen atoms in blue and fluorine atoms in maroon)

reveals that (a) co-substitution of N and F is preferred over individual substitution with N or F, with a lowering of energy by 1.97 eV/atom, and (b) further substitution of N in N,F-ZnO is also favorable with a lowering of energy by 0.61 eV/atom. The energies of different chemically ordered configurations of N,F-ZnO reveal that (a) N and F preferentially occupy nearest neighbour sites bonded via a cation (Zn), (b) configurations with N anions occupying the nearest neighbour sites are not energetically favorable. Thus, the tendency of N and F to cluster together is evident, and not surprising, as the combination of electrostatic and covalent interactions would favor this ordering.

4.3.2 Electronic Structure

Our calculated band structure of bulk ZnO (see Figure 4.3) is in good agreement with previous LDA calculations [48]. While the energy gaps obtained from the Kohn-Sham spectrum within DFT are always underestimated, the severe underestimation of the gap in ZnO (to ∼0.84 eV, in comparison with the experimental gap of 3.37 eV) is partly due to strong interactions between p-states of oxygen and the fully occupied d-states of Zn, both of which are close in energy [49]. Self-interaction corrected calculations within a GW approximation using ESPRESSO and ABINIT improved the gap through an increase of about 0.6 and 0.7 eV respectively. We note that the underestimation of the gap of ZnO even with GW calculations is probably due to the use of pseudopotentials, as all-electron based calculations within GW approximation gave a better estimation of the gap (2.44 eV) in ZnO [50], though there is some scatter in these results as well. Since the improvement in the gap with these calculations is not particularly significant, we present first-principles analysis of the electronic structure of N and F-co-substituted ZnO within the standard DFT calculations, and interpret our results keeping in mind the underestimation of gaps. The calculated band structure of a representative configuration of N,F-co-substituted ZnO (see Figure 4.3) shows an isolated band split above and weakly from the rest of the valence bands. It gives rise to a considerable reduction in the gap of bulk ZnO (Δ ∼0.67 eV).

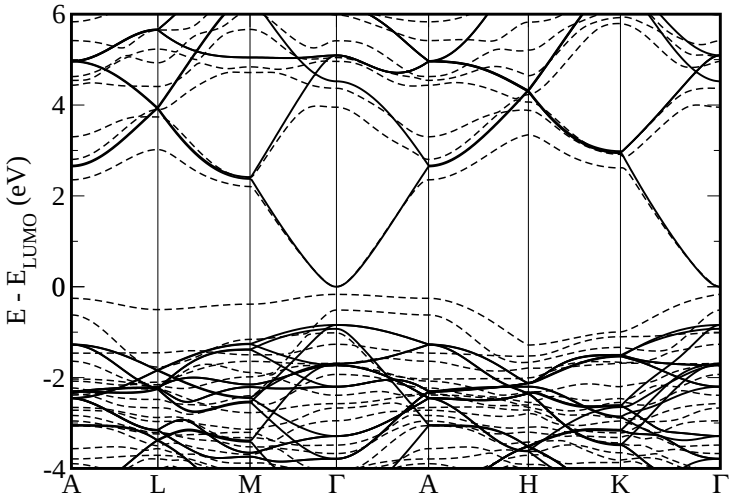

Figure 4.3: Comparison of the electronic band structures of bulk (contiguous line) and a representative configuration of N, F-ZnO (dotted line), obtained from DFT-based calculations

4.3.3 Nature of the Sub-band

To understand the nature of this sub-band at the top of the valence band originating from N,F-co-substitution, we analyzed the density of electronic states of bulk ZnO and N,F-ZnO, projecting it onto atomic orbitals. In bulk ZnO (see Figure 4.4a), the valence band is constituted primarily of O $2p$ states with notable mixing with Zn $3d$ states, while the low energy conduction bands have a predominant character of Zn $4s$ states. First of all, relatively sharp peaks in the valence bands seen in the electronic density of states of bulk ZnO get broadened or diffused upon substitution of N and F for O and associated disorder at anion sites (see Figure 4.4b). Undoubtedly, the uppermost valence bands are the most affected by the N,F-co-substitution, with N $2p$-derived states arising as a sub-band at the top of the valence

band (with minor contributions from the Zn $3d$ and O $2p$-derived states), effectively reducing the band gap. Visualization of the uppermost valence states at the Γ-point (inset in Figure 4.4b) shows that its charge is localized largely on the N atoms, and spreads weakly onto the p-orbitals of O and d-orbitals of Zn atoms. From the electronic density of states of F-ZnO, N-ZnO and N,F-ZnO, we find that (a) p-states of the strongly electronegative F are deep down in energy, while those of less electronegative N are concentrated at the top of the valence band, and (b) p-states of additional N (in N,F-ZnO) form the sub-band just above the valence band. Thus, the reduction in the gap is indeed an effect of co-substitution of F and N, as F enhances the effect of N-substitution. The lowest energy conduction bands with Zn $4s$-character are essentially unaffected by the substitution.

4.3.4 Statistical Averaging: Temperature Dependence

Since we considered all the chemically ordered configurations possible in the supercell, we now carry out statistical averaging to estimate the decrease in band gap as a function of temperature at which the sample is annealed in synthesis (note that this is not the temperature of measurement):

$$\left\langle \Delta E_g(T) \right\rangle = \frac{\sum_c m_c \; e^{\frac{-E_c}{k_B T}} \; \Delta E_g^c}{\sum_c m_c \; e^{\frac{-E_c}{k_B T}}} \tag{4.1}$$

where m_c is the multiplicity of configuration c, E_c is the energy of configuration c relative to the one with the lowest total energy, ΔE_g^c is the change in the band gap for configuration c relative to bulk ZnO, k_B is the Boltzmann

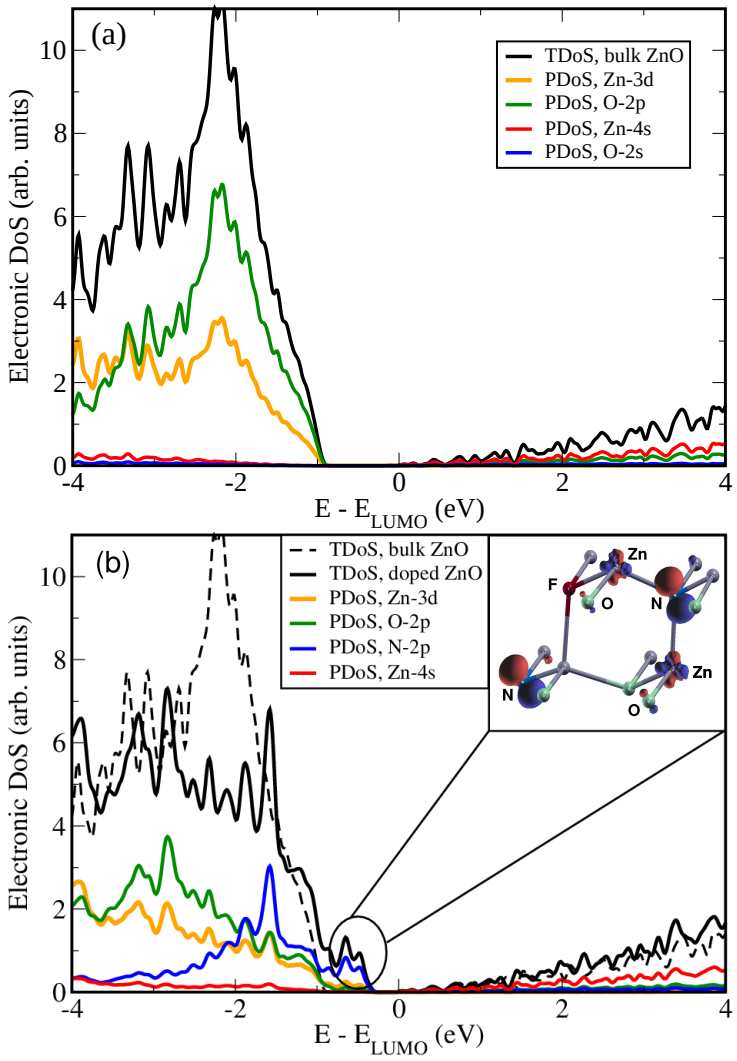

Figure 4.4: Partial density of electronic states of a) bulk ZnO and b) a representative configuration of N,F-ZnO, obtained from DFT-based calculations. The inset in (b) is a visualization of the valence states of the N, F-ZnO configuration

constant and T is the temperature. From the change in the band gap of N,F-ZnO as a function of temperature used in synthesis (see Figure 4.5), the largest reduction in the effective band gap occurs at a synthesis temperature

of around 500 K

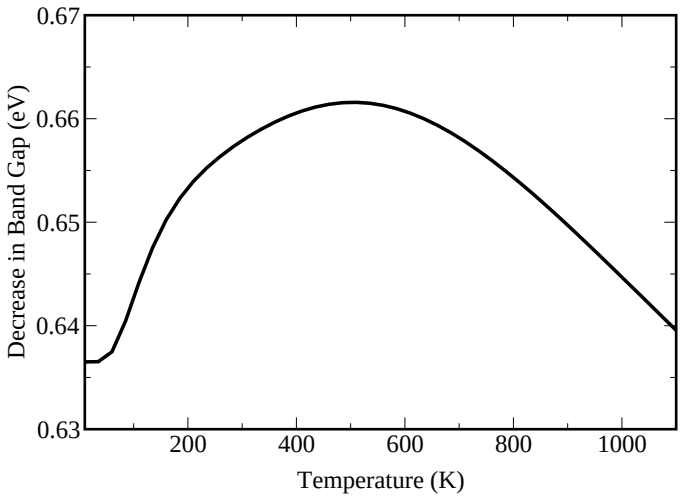

Figure 4.5: Decrease in the band gap of N,F-ZnO as a function of synthesis temperature, obtained from DFT-based calculations, statistically averaged according to Equation 4.1

4.3.5 Optical Absorption

We have determined the optical absorbance from the electronic structure of ZnO and N,F-co-substituted ZnO (see Figure 4.6). The effect of the N sub-band is indeed clear in the absorption at energies below the band gap of bulk ZnO, consistent with the experiments here. Due to the error in band gap, we have used a scissor correction to align the absorption edge of bulk ZnO with that measured in experiment.

Changes in the electronic structure with N,F-co-substitution, particularly the reduction in the band gap is reflected in the changes in its properties such as dielectric constant. The electronic dielectric constant (ϵ^{∞}) estimated

using DFT-based linear response calculations show two to three-fold increase with N,F-co-substitution (from about 8.9 to 20.3).

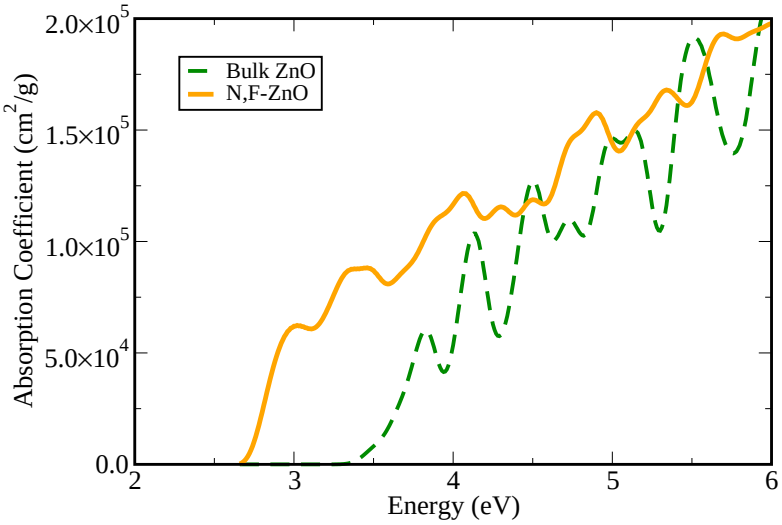

Figure 4.6: Comparison of the absorption coefficients of bulk and N,F-ZnO. A scissor correction of ∼2.5 eV has been applied.

4.3.6 Vibrations of N,F-ZnO

We now determine the vibrational signatures of N,F-co-substitution in ZnO by examining the vibrational density of states (DoS) of bulk and substituted ZnO (see Figure 4.7) obtained with linear response calculations using ESPRESSO. Our estimates of the phonon frequencies of bulk ZnO are in good agreement with the observed Raman spectrum. It is seen that the peaks at 90, 410 and 445 cm^{-1} correspond to the modes with polarization (atomic displacements) in the *ab* plane whereas those at 260, 390 and 550 cm^{-1} involve displacements along the *c*-axis. The vibrational DoS of a representative configuration of N,F-ZnO (see Figure 4.7) shows (a) overall hardening of the

modes, and (b) additional peaks which arise due to Brillouin zone folding associated with the supercell, and they too agree well with the observed Raman spectrum. A detailed examination of the eigenvectors of these modes reveals that the peaks at 240, 490, 530 and 600 cm^{-1} correspond to displacements of the substituted N atoms along the *c*-axis.

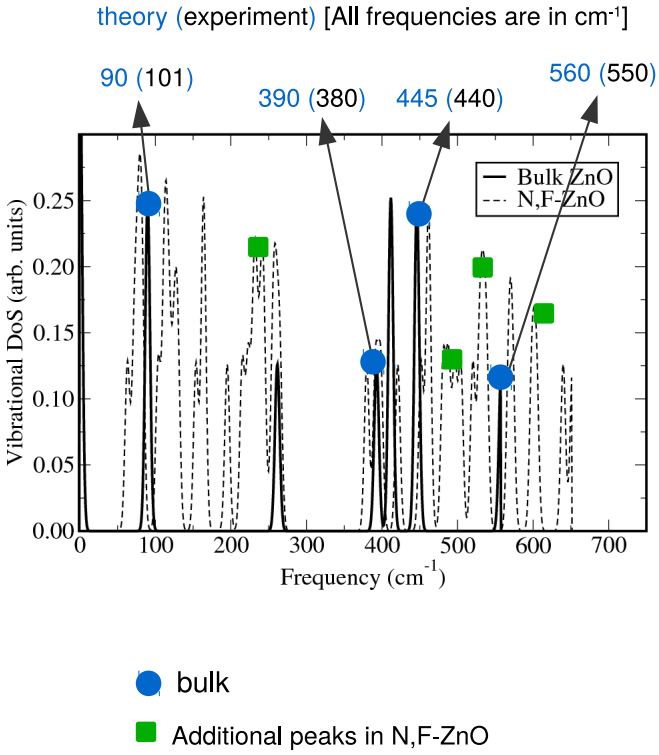

Figure 4.7: Comparison of vibrational density of states (DoS) of bulk and N,F-ZnO, obtained from ESPRESSO-based linear response calculations

4.4 Summary

Our calculations show that co-substitution of N and F for O in ZnO is preferred over individual substitution by N or F, and it involves pairing of N

and F at neighbouring sites with the resulting bonds being stiffer than those of pure ZnO. *p*-orbitals of nitrogen are the most effective states in altering the electronic structure of ZnO by giving rise to a sub-band of about 0.6 eV bandwidth, at the top of the valence band, thus effectively reducing the band gap of ZnO, and their effect is enhanced by the presence of fluorine. While our calculations underestimate the gap and the changes in it, they provide a clear picture of the effect of N and F co-substitution on the electronic structure of ZnO.

Chapter 5

Structure, Electronic and Catalytic Properties of TiO_2 Co-substituted with Nitrogen and Fluorine*

"Will mankind one day without the net expenditure of energy be able to restore the sun to its full youthfulness even after it had died of old age?"

- Isaac Asimov, *The Last Question*

5.1 Introduction

Increasing energy demands and rapid consumption of fossil fuels have motivated a great deal of research on materials capable of producing hydrogen by the reduction of water. Among them, titanium oxide (TiO_2) has been an important material because of its high chemical and photo-stabilities, non-toxicity and abundance. A limitation, however, is that the visible region

*Reproduced in part with permission from *Inorganic Chemistry*, accepted for publication. Unpublished work copyright 2013 *Americal Chemical Society*.

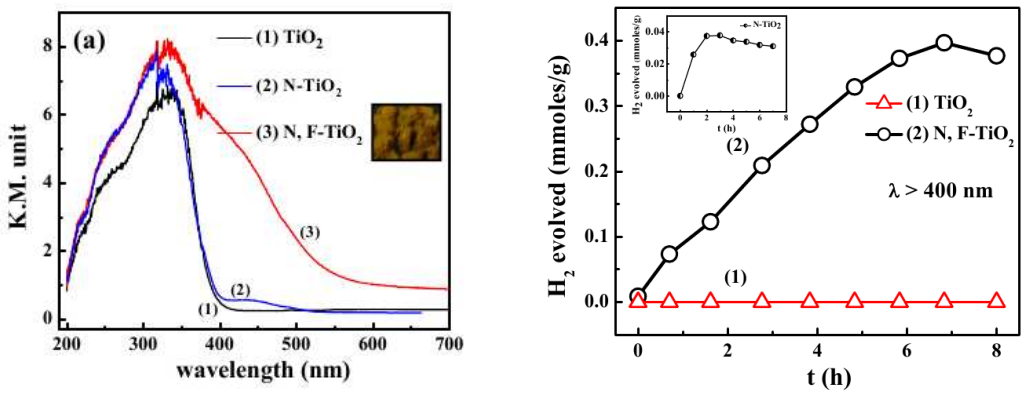

Figure 5.1: (a) UV-Visible spectra of undoped, N-doped and N,F-co-doped TiO_2; the inset shows the colour of N,F-TiO_2. (b) Hydrogen evolution with respect to time on irradiation with visible light (> 400 nm) for undoped and N,F-co-doped TiO_2; inset shows the data for N-doped TiO_2. (Images: courtesy Prof. C. N. R. Rao's group, ICMS, JNCASR)

of the solar spectrum cannot be used with TiO_2 due to its high band gap (indirect, E_g = 3.23 eV). Considerable amount of work has been carried out in order to extend the absorption of TiO_2 to the visible region. Towards this end, Prof. C. N. R. Rao's group here[†] synthesized TiO_2 heavily co-substituted with nitrogen and fluorine (N,F-TiO_2), and observed (a) a significant reduction in the band gap accompanied by yellow colouration (See Figure 5.1a), and (b) a significant increase in the photocatalytic water splitting capabilities to produce hydrogen (see Figure 5.1b). We try to understand here the effect of nitrogen and fluorine co-substitution on the structure and electronic properties of TiO_2 at the atomistic level.

Titanium dioxide or titania occurs in nature primarily as minerals rutile, anatase and brookite. The rutile phase is the most abundant and

[†]International Centre for Materials Science, Jawaharlal Nehru Centre for Advanced Scientific Research

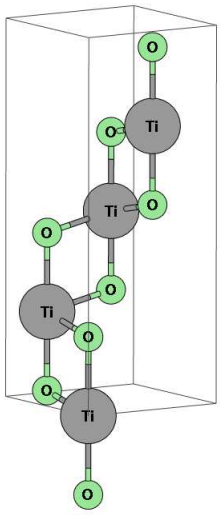

Figure 5.2: Conventional unit cell of anatase TiO_2 with four formula units

the metastable anatase and brookite phases convert to rutile upon heating. Nonetheless, the anatase polymorph (studied here) is a better catalyst and is used more widely in (photo)electrochemistry. Anatase TiO_2 crystallizes in a tetragonal lattice (space group 141 or $I4_1/amd$) with four formula units in the unit cell (See Figure 5.2), and with lattice constants $a = 3.7845$ Å, $c = 9.5143$ Å [51]. The atomic basis is given by:

$$\text{Ti: } \left\{(0,\,0,\,0),\,(0,\,\tfrac{1}{2},\,\tfrac{1}{4}),\,(\tfrac{1}{2},\,\tfrac{1}{2},\,\tfrac{1}{2}),\,(\tfrac{1}{2},\,0,\,\tfrac{3}{4})\right\}$$

$$\text{O: } \left\{(0,\,0,\,u),\,(0,\,\tfrac{1}{2},\,\tfrac{1}{4}+u),\,(\tfrac{1}{2},\,\tfrac{1}{2},\,\tfrac{1}{2}+u),\,(\tfrac{1}{2},\,0,\,\tfrac{3}{4}+u),\right.$$
$$\left.(0,\,0,\,-u),\,(0,\,\tfrac{1}{2},\,\tfrac{1}{4}-u),\,(\tfrac{1}{2},\,\tfrac{1}{2},\,\tfrac{1}{2}-u),\,(\tfrac{1}{2},\,0,\,\tfrac{3}{4}-u)\right\}$$

5.2 Computational Methods

Our first-principles calculations are based on density functional theory as implemented in the (a) Quantum ESPRESSO [42], and (b) SIESTA [41]

packages. In our ESPRESSO-based calculations, ultrasoft pseudopotentials [26] were used to model the interaction of ionic cores with electrons and the exchange-correlation energy functional was approximated with a local density approximation (LDA) of the Perdew-Zunger form [52]. Kinetic energy cutoffs of 50 Ry and 400 Ry were used for the representation of wavefunctions and charge density respectively. Phonons and Born effective charges were calculated as second derivatives of energy within density functional perturbation theory (DFPT). Since the electronic band gap is underestimated in DFT-LDA calculations, we used hybrid density functionals based on a screened Coulomb potential for Hartree-Fock exchange (HSE) [53], to obtain more accurate estimates of the band gap, and quantitatively confirm the experimental observations. Since ESPRESSO-based calculations were computationally expensive, we used SIESTA in our analysis of water adsorption on the (001) and (101) surfaces of nitrogen and fluorine co-substituted TiO_2. In the SIESTA-based calculations, we use Troullier-Martins [45] pseudopotentials to model ion-electron interactions and approximate the exchange-correlation energy functional with a Ceperly-Alder form [46] of LDA. We use atomic orbitals of multiple-zeta kind with a split valence scheme as the basis with a split norm of 0.15, and the orbital-confining cutoff radii defined by an energy shift of 0.007 Ry.

We considered three kinds of anionic substitution in TiO_2 in the analysis: a) nitrogen substituted TiO_2 (N-TiO_2), (b) fluorine substituted TiO_2 (F-TiO_2), and (c) nitrogen and fluorine *co-substituted* TiO_2 (N,F-TiO_2), for a comparative study the effects of co-substitution with nitrogen and fluorine with respect to their individual substitution. To simulate the doping levels

achieved in experiments here, we used a 2×2×1 periodic supercell with 48 atoms ($Ti_{16}O_{32}$) with substitution of (a) 2 of the oxygen atoms with nitrogen atoms (6.25% N) for N-TiO_2, (b) 2 of the oxygen atoms by fluorine atoms (6.25% F) for F-TiO_2, and (c) 4 of the oxygen atoms with 2 nitrogen atoms and 2 fluorine atoms (6.25% F, 6.25% N) for N,F-TiO_2. Since the number of possible configurations of ordering of nitrogen and fluorine in these systems is very large, we used one representative configuration in each case, except in the case of N,F-TiO_2 where we compared a few distinct configurations to determine the nature of ordering preferred by nitrogen and fluorine. In our calculations on water splitting on (001) and (101) surfaces using SIESTA, we used a single-layer slab of N, F-TiO_2 with 2×2 surface cells, and a vacuum of ∼15 Å. A water molecule was placed parallel to the surface with its oxygen about 2.2 Å above a 5-coordinated Ti site (referred to as 'Ti(5c)'), and the substituted nitrogen atom lying close to the surface. To sample integrations over the Brillouin-zone of the supercell, we used a uniform k-mesh of 5×5×4 in ESPRESSO based calculations, and 2×6×2 (for the (101) surface) and 4×4×1 (for the (001) surface) in SIESTA based calculations. In all cases, structural relaxation was carried out through energy minimization until the Hellman-Feynman forces on the atoms were within 0.05 eV/Å, and the stresses were within 1 kbar.

5.3 Results and Discussion

5.3.1 Lattice Parameters and Local Distortions

Our calculated lattice parameters of bulk anatase TiO_2 are a = 3.74 Å, c = 9.42 Å, u = 0.209, within typical LDA errors and in good agreement with the experimental and published theoretical values [51, 54]. The change in lattice parameters upon substitution with nitrogen and fluorine at oxygen sites is small (within 0.9% of those calculated for bulk TiO_2). On the other hand, there are significant local structural distortions in N,F-TiO_2 induced at the sites of substitutions (see Figure 5.3a). The Ti-N bond length along the *c*-axis is 1.82 Å while that of the Ti-F bond is 2.40 Å. Notably, these are 7.5% shorter and 22.3% longer, respectively, relative to the Ti-O bonds (1.96 Å) in bulk TiO_2. The changes in the bond lengths of Ti-N and Ti-F bonds along the *ab*-plane are relatively less dramatic and are about 3.7% and -1.5% respectively. These lead to smaller Ti-N-Ti (143.2°) and larger Ti-F-Ti (177.6 °) bond angles, in comparison with Ti-O-Ti bond angles in bulk TiO_2 (156.4°) (see Figure 5.3b). These structural changes suggest that the behaviour of nitrogen and fluorine is like negative and positive charges respectively in N,F-TiO_2. It is observed that these local distortions are much more pronounced in N,F-TiO_2 than in the case of F-TiO_2 and N-TiO_2, indicating that nitrogen and fluorine co-substitution reinforces the effects of their substitution individually and gives greater stability.

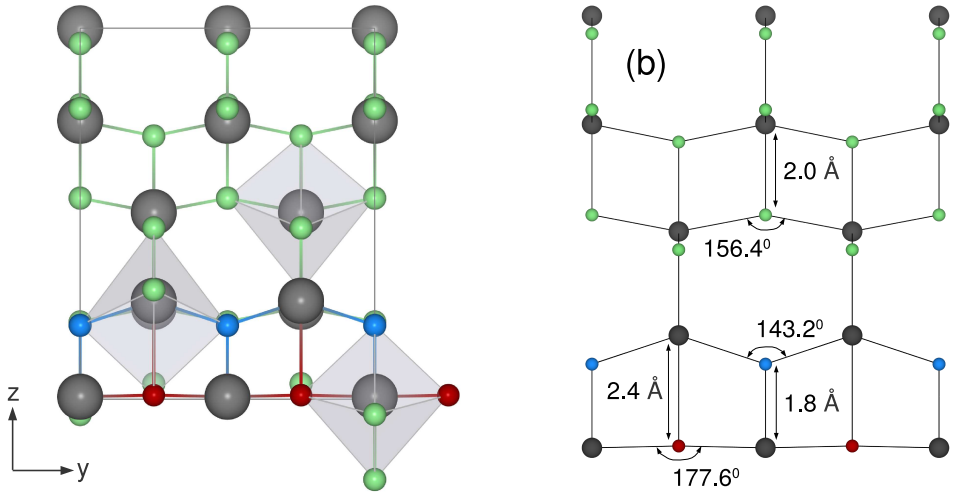

Figure 5.3: Structure of N,F-TiO_2 showing (a) Ti in three differently coordinated octahedral environments, (b) the local distortions caused by nitrogen and fluorine co-substitution (Ti = grey, O = green, N = blue, F = maroon).

5.3.2 Chemical Ordering

The energetics of N-TiO_2, F-TiO_2 and N,F-TiO_2 reveal that (a) co-substitution with nitrogen and fluorine is preferred over their individual substitution with a lowering of energy by 1.93 eV per (N,F) pair, and (b) further substitution with excess nitrogen in N,F-TiO_2 is also favorable with a lowering of energy by 1.59 eV for an additional substituted nitrogen. The energies of different chemically ordered configurations of N,F-TiO_2 (with additional nitrogen substitution) suggest that (a) nitrogen and fluorine prefer nearest neighbour sites, being bonded to a cation (Ti), and (b) two nitrogen (or two fluorine) anions occupying such nearest neighbour sites is energetically unfavorable. This observation is not unexpected, as the nature of electrostatic interactions between nitrogen and fluorine would favor this pair-wise clustering behaviour.

5.3.3 Electronic Structure

The local structural changes at the substituted nitrogen and fluorine sites in TiO_2 are reflected in the electronic structure. The electronic charge density contours (see Figure 5.4) clearly reveal (a) a greater covalency in the Ti-N bond, and that the chemical environment around nitrogen is quite anisotropic, (b) the spherical symmetry of the charge around fluorine, which reflects that the electronic orbitals of fluorine are completely filled, and the associated bonding is mostly ionic in nature, and (c) weakening (lengthening) of the bond between oxygen and the Ti that is bonded to N with a relatively strong and covalent Ti-N bond.

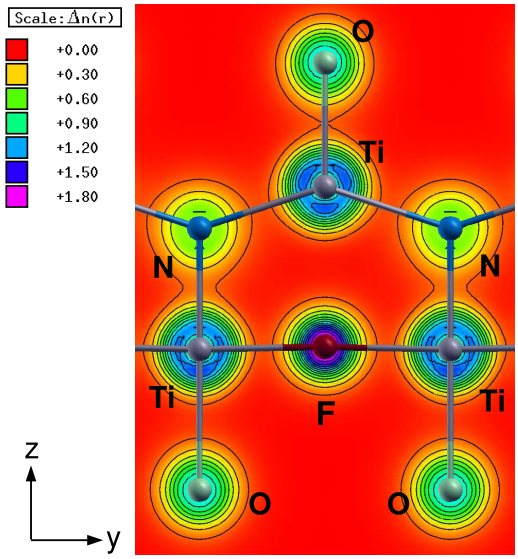

Figure 5.4: Contours of electronic charge density on the (100) plane of N,F-TiO_2

Our calculated band structure of bulk TiO_2 (see Figure 5.5a) is in good agreement with published LDA calculations [54], with an indirect band

gap of 2.06 eV at 0.29 Σ (in the Γ to X direction) comparable to earlier theoretical estimates [55]. Underestimation of the band gap with respect to the reported experimental value of 3.23 eV is typical of the calculation based on DFT-LDA functional. Band structure of a representative N,F-TiO_2 (see Figure 5.5b) shows an isolated occupied band split weakly from the rest of the valence bands, leading to a direct and considerably reduced gap of 1.48 eV at Γ. From our hybrid exchange functional calculations on a 2×2×1 mesh of Bloch vectors, we estimate the correction to the band gaps and add it to our LDA estimates obtained using a much finer mesh of k-vectors. Thus corrected band gaps of pure TiO_2 (3.92 eV) and N,F-TiO_2 (3.06 eV) are sort of overestimated in comparison with the experimentally measured values (3.20 eV and 2.28 eV, respectively) but they succeed in capturing more accurately the change in the band gap upon nitrogen and fluorine co-substitution. This reduction in the electronic band gap is essential and partially responsible for the improved photocatalytic activity of TiO_2 after co-substitution with nitrogen and fluorine (we will see in Section 5.3.6).

5.3.4 Nature of the Sub-band

To understand the nature of the isolated sub-band at the top of the valence band, we analyzed the density of electronic states of bulk TiO_2 and N,F-TiO_2, by projecting it onto atomic orbitals. In bulk TiO_2, the valence band is constituted primarily of O $2p$ orbitals with a little mixing with the Ti $3d$ states while the lowest energy conduction bands are predominantly Ti $3d$ in

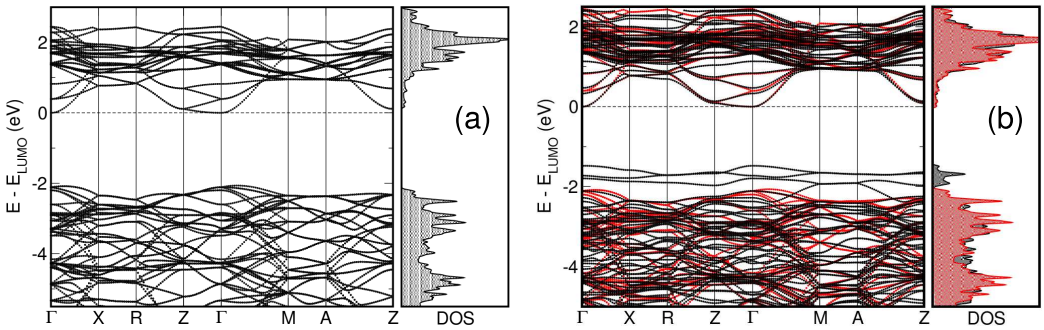

Figure 5.5: Electronic band structure of bulk, undoped TiO_2, and (b) comparison of the band structures of pure TiO_2 (in red) and N,F-TiO_2 (in black). The N 2*p*-derived sub-band above the valence band is clearly visible.

character (see Figure 5.6a). The uppermost valence bands are most affected by the N,F-co-substitution, with N 2*p* derived states arising as a sub-band with a bandwidth of about 0.6 eV, at the top of the valence band (with weaker contributions from the Ti 3*d* and the O 2*p* derived states), effectively reducing the band gap (see Figure 5.6b). Our analysis of the density of electronic states of N-TiO_2, F-TiO_2 and N,F-TiO_2 reveals that (a) *p* states of the strongly electronegative fluorine atoms are deep-lying in energy ($\sim$ 6 eV lower than the valence band maximum; see Figure 5.6b) while those of less electronegative nitrogen are concentrated at the top of the valence band, and (b) formation of the sub-band of *p* states of the nitrogen atoms (in N,F-TiO_2) at the top of the valence band is greatly enhanced by the fluorine co-substitution (see the inset in Figure 5.6b). The lowest energy conduction bands are essentially unaffected by N,F co-substitution and retain their Ti 3*d* character.

From the visualization of the uppermost valence states at the Γ-point

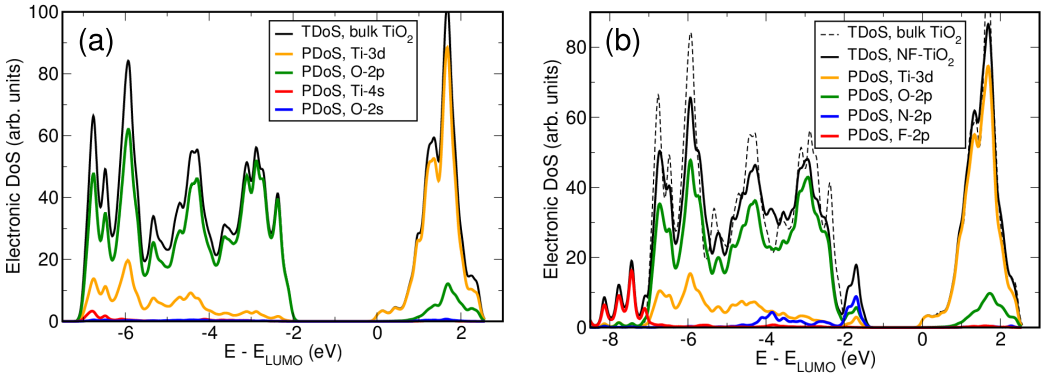

Figure 5.6: Density of electronic states projected onto atomic orbitals in (a) bulk, undoped TiO_2, and (b) N,F-co-substituted TiO_2. The inset in (b) is a comparison between the total density of electronic states (at the top of the valence band) of N-TiO2 and N,F-TiO_2, clearly showing the enhancement in the sub-band due to fluorine co-substitution.

we confirm that the charge is localized largely on the nitrogen atoms, and spread weakly onto the p orbitals of the nearest neighbour oxygen atoms (see Figure 5.7). The nature of this wavefunction reveals a weak covalent π-interaction between p_x-orbital of oxygen and d_{xz} orbital of Ti.

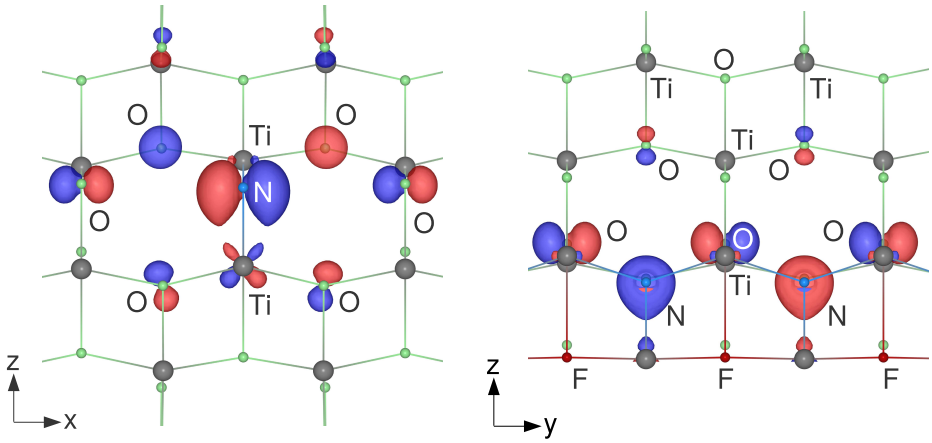

Figure 5.7: Visualization of the uppermost valence states of N,F-TiO_2 from y-direction (left) and x-direction (right) (Ti = grey, O = green, N = blue, F = maroon)

5.3.5 Born Effective Charges

The Born effective charge (BEC) tensor $Z^*_{i,\alpha\beta}$ [56] of an atom in an insulator is defined as the atomic displacement ($u_{i,\beta}$) derivative of polarization $\mathcal{P}$:

$$Z^*_{i,\alpha\beta} = \frac{\partial \mathcal{P}_\alpha}{\partial u_{i,\beta}} \tag{5.1}$$

where i runs over the atoms and α, β are Cartesian indices. The anomalous BECs of Ti in bulk TiO_2 ($Z^*_{xx} = Z^*_{yy} = 6.5$, $Z^*_{zz} = 5.7$) when compared to its nominal ionic charge of +4 is indicative of the hybridization of its d-states with the p-states of the surrounding oxygen ions, and reflects a mixed covalent-ionic picture of bonding [57]. The anomalous BECs of oxygen (Z^*_{xx} = -1.2, Z^*_{yy} = -5.4, Z^*_{zz} = -2.9) in comparison with its nominal charge of -2 reveals a deviation from the purely ionic nature and a high anisotropy associated with the site, confirming our earlier conclusions based on the analysis of electronic density. In N,F-TiO_2, the BECs of nitrogen are Z^*_{xx} = -1.2, Z^*_{yy} = -5.8, Z^*_{zz} = -3.9, while those of fluorine are Z^*_{xx} = -0.7, Z^*_{yy} = -3.2, Z^*_{zz} = -1.1. This is consistent with the Ti-N-Ti and Ti-F-Ti chains seen along the y direction and the π-like bonding interaction between Ti-3d states and N-2p states in the z direction. It is to be noted that the anomaly in the BEC tensor of Ti is stronger when it is bonded to nitrogen and weaker when bonded to fluorine. This clearly shows a significant chemical activity of N and relative inertness of F, and confirms the mixed ionic-covalent and ionic nature of Ti-N and Ti-F bonds respectively. Our calculations show an increase in the z-component of the electronic dielectric constant (the square

of the refractive index) from 6.2 to 6.5, as another effect of reduction in the electronic band gap on properties.

5.3.6 Water adsorption on (001) and (101) surfaces

In the case of pure anatase TiO_2, molecular adsorption of water occurs on the (101) surface while dissociative adsorption is favoured on the (001) surface [58]. We have studied here the effect of nitrogen and fluorine co-substitution on the nature of interaction of water with (001) and (101) surfaces of TiO_2. In both cases, we find that the strength of water molecules to adsorb on these surfaces increases significantly upon co-substitution with nitrogen and fluorine, reflected in the increase in adsorption energies: from ∼1.6 eV [58] to ∼3.6 eV for the (001) surface, and from ∼0.7 eV [58] to ∼2.0 eV for the (101) surface.

Moreover, in the case of (001) surface of N,F-TiO_2, we find that there is formation of an intermediate complex, characterized by a weakened bond (3.11 Å) between an oxygen (fluorine) atom and the Ti(5c) atom involved in the adsorptive interaction. As a result, this activated oxygen (fluorine) forms a bond (1.04 Å) with a hydrogen atom of the water molecule (see Figure 5.8a). The O-H bond lengths of the strained water molecule are 0.97 Å and 1.44 Å, the latter hydrogen being bonded to the activated oxygen (fluorine) atom. This is the intermediate state preempting the dissociation of the water molecule.

In the case of the (101) surface too, we observe structural changes contributing towards enhanced catalytic activity: a water molecule relaxes

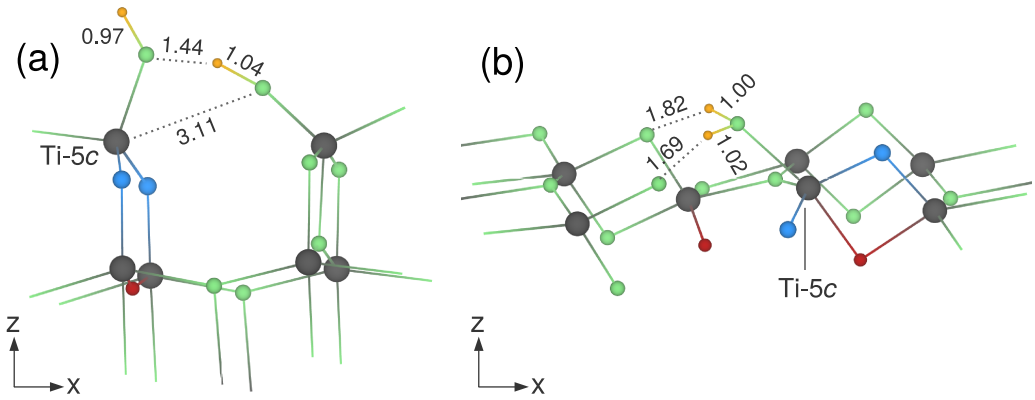

Figure 5.8: Interaction of a water molecule with the (a) (001) surface, and (b) (101) surface of N,F-TiO_2. (All bond lengths shown are in Å. Ti = grey, O = green, N = blue, F = maroon, H = orange).

to a position favoring bonding interaction between its hydrogen atoms and two neighbouring oxygen (fluorine) atoms on the surface (with O-H bond lengths of 1.69 Å and 1.82 Å). The corresponding O-H bond lengths of the strained water molecule are 1.02 Å and 1.00 Å (in contrast with 0.97 Å for an isolated molecule), making it relatively easier to photolyse. The chemical origin of these structural changes lies in the relatively stronger bond between the Ti(5c) atom and a nitrogen atom substituted at the neighbouring site, leading to weakening of the Ti(5c)-O(F) bond (see our analysis based on charge density, in Section 5.3.3). The latter is broken with ease and the oxygen (fluorine) atom bonds with a hydrogen atom of the water molecule.

Thus, a weaker Ti(5c)-O(F) bond and the associated structural changes contribute towards relatively enhanced water dissociation capabilities of N,F-TiO_2. Secondly, the sub-band due to N-2*p* derived states at the top of the

valence band, further pronounced by fluorine co-substitution, facilitates absorption of a photon and subsequent electron transfer to a water molecule, thereby increasing the ease with which water is split into hydrogen and oxygen. These factors, combined with the reduced electronic band gap, result in the enhancement of the photocatalytic activity of TiO_2 upon co-substitution with nitrogen and fluorine.

5.4 Summary

Our calculations show that nitrogen and fluorine co-substitution in TiO_2 leads to significant local structural distortions associated with a strong bonding interaction of nitrogen with titanium, which is reflected in (a) the anomalous Born effective charges, and (b) an electronic sub-band of N-2p orbitals that appears at the top of the valence band. The latter is responsible for a significant reduction in the band gap of the material (0.58 eV in LDA, 0.86 eV in HSE calculations). Our calculations of water adorption on the (001) and (101) surfaces of N,F-TiO_2 reveal that a strong Ti interaction with the neighbouring nitrogen leads to the weakening of its bond with the neighbouring anion (O or F, the activated site), facilitating a bonding interaction between the activated anion and a hydrogen of the adsorbed water molecule. This and the reduction in the electronic band gap are cumulatively responsible for the enhanced photocatalytic activity of N,F-TiO_2 towards splitting of water.

Chapter 6

Conclusion

"So long and thanks for all the fish."

- Douglas Adams, *The Hitchhiker's Guide to the Galaxy*

This work has focused on the usage of first-principles theory to explain certain puzzling material behaviour observed in experiments. Using density functional theory (DFT) and density functional tight binding (DFTB) based calculations as a theoretical microscope, atomistic mechanisms for the bizarre experimental observations have been detailed.

We have studied the complete nonlinear elastic response of a metal organic framework, ZIF-8, to mechanical shear stress. We identify a Raman signature of stacking faults arising out of shear deformation as splitting of a peak at $\sim$1280 cm^{-1} into two peaks at $\sim$ 1260 cm^{-1} and $\sim$1230 cm^{-1}. We indentify the atomistic mechanism by which only Zn-N bonds get broken and reformed during the formation of such low-energy faults. We explain the lack of evidence for such faults in experiments by the preferential formation of a high density amorphous phase through the release of shear and compressive stresses acting on the barrier for the formation of an intrinsic fault.

We study the effects of heavy nitrogen and fluorine co-substitution on functional oxides, zinc oxide and titanium oxide, including changes in their structure, electronic, optical and catalytic properties. We identify in both cases that nitrogen derived p-states give rise to a sub-band above the valence states, effectively reducing the band gap to a significant extent, this effect being enhanced by the presence of fluorine. This effect is also reflected in the calculated optical absorption spectra and dielectric constants. Our calculations on the water adsorption on anatase surfaces reveal that a strong bonding interaction between titanium and nitrogen facilitates the formation of a bond between a hydrogen of the water molecule and an activated anion, enhancing its photocatalytic activity.

Bibliography

[1] M. Castells, *The Rise of the Network Society: The Information Age: Economy, Society, and Culture Volume I.* Wiley-Blackwell, 2nd ed., 2009.

[2] C. Liu, F. Li, L.-P. Ma, and H.-M. Cheng, "Advanced materials for energy storage," *Advanced Materials*, vol. 22, pp. E28–E62, 2010.

[3] M. S. Dresselhaus and I. L. Thomas, "Alternative energy technologies," *Nature*, vol. 414, pp. 332–337, 2001.

[4] C. Chappert, A. Fert, and F. N. V. Dau, "The emergence of spin electronics in data storage," *Nat. Mater.*, vol. 6, pp. 813–823, 2007.

[5] R. Langer and D. A. Tirrell, "Designing materials for biology and medicine," *Nature*, vol. 428, pp. 487–492, 2004.

[6] M. D. Segall, P. J. D. Lindan, M. J. Probert, C. J. Pickard, P. J. Hasnip, S. J. Clark, and M. C. Payne, "First-principles simulation: ideas, illustrations and the CASTEP code," *J. Phys. Condens. Matter*, vol. 14, p. 2717, 2002.

[7] R. M. Martin, *Electronic Structure: Basic Theory and Practical Methods.* Cambridge University Press, 2004.

[8] M. C. Payne, M. P. Teter, D. C. Allan, T. A. Arias, and J. D. Joannopoulos, "Iterative minimization techniques for *ab initio* total-energy calculations: molecular dynamics and conjugate gradients," *Rev. Mod. Phys.*, vol. 64, pp. 1045–1097, 1992.

[9] J. P. Perdew, K. Burke, and M. Ernzerhof, "Generalized gradient approximation made simple," *Phys. Rev. Lett.*, vol. 77, pp. 3865–3868, Oct 1996.

[10] M. Elstner, D. Porezag, G. Jungnickel, J. Elsner, M. Haugk, T. Frauenheim, S. Suhai, and G. Seifert, "Self-consistent-charge density-functional tight-binding method for simulations of complex materials properties," *Phys. Rev. B*, vol. 58, p. 7260, 1998.

[11] R. Morris and P. Wheatley, "Gas Storage in Nanoporous Materials," *Angew. Chem. Int. Ed.*, vol. 47, pp. 4966–4981, 2008.

[12] J.-R. Li, R. J. Kuppler, and H.-C. Zhou, "Selective gas adsorption and separation in metal-organic frameworks," *Chem. Soc. Rev.*, vol. 38, pp. 1477–1504, 2009.

[13] J. Lee, O. K. Farha, J. Roberts, K. A. Scheidt, S. T. Nguyen, and J. T. Hupp, "Metal-organic framework materials as catalysts," *Chem. Soc. Rev.*, vol. 38, pp. 1450–1459, 2009.

[14] M. D. Allendorf, C. A. Bauer, R. K. Bhakta, and R. J. T. Houk, "Luminescent Metal-Organic Frameworks," *Chem. Soc. Rev.*, vol. 38, pp. 1330–1352, 2009.

[15] O. R. Evans and W. Lin, "Crystal Engineering of NLO Materials Based on Metal-Organic Coordination networks," *Acc. Chem. Res.*, vol. 35, pp. 511–522, 2002.

[16] P. Horcajada, T. Chalati, C. Serre, B. Gillet, C. Sebrie, T. Baati, J. F. Eubank, D. Heurtaux, P. Clayette, C. Kreuz, J.-S. Chang, Y. K. Hwang, V. Marsaud, P.-N. Bories, L. Cynober, S. Gil, G. Ferey, P. Couvreur, and R. Gref, "Porous metal-organic framework nanoscale carriers as a potential platform for drug delivery and imaging," *Nat. Mater.*, vol. 9, pp. 172–178, 2010.

[17] J. C. Tan and A. K. Cheetham, "Mechanical Properties of Hybrid Inorganic-Organic Framework Materials: Establishing Fundamental

Structure-Property Relationships," *Chem. Soc. Rev.*, vol. 40, pp. 1059–1080, 2011.

[18] S. Moggach, T. Bennett, and A. Cheetham, "The effect of pressure on ZIF-8: increasing pore size with pressure and the formation of a high-pressure phase at 1.47 GPa," *Angew. Chem. Int. Ed.*, vol. 48, pp. 7087–7089, 2009.

[19] J. C. Tan, T. D. Bennett, and A. K. Cheetham, "Chemical Structure, Network Topology, and Porosity Effects on the Mechanical Properties of Zeolitic Imidazolate Frameworks," *Proc. Natl. Acad. Sci. USA*, vol. 107, pp. 9938–9943, 2010.

[20] J.-C. Tan, B. Civalleri, C.-C. Lin, L. Valenzano, R. Galvelis, P.-F. Chen, T. D. Bennett, C. Mellot-Draznieks, C. M. Zicovich-Wilson, and A. K. Cheetham, "Exceptionally Low Shear Modulus in a Prototypical Imidazole-Based Metal-Organic Framework," *Phys. Rev. Lett.*, vol. 108, p. 095502, 2012.

[21] S. Cao, T. D. Bennett, D. A. Keen, A. L. Goodwin, and A. K. Cheetham, "Amorphization of the Prototypical Zeolitic Imidazolate Framework ZIF-8 by Ball-milling," *Chem. Commun.*, vol. 48, pp. 7805–7807, 2012.

[22] A. A. Griffith, "The Phenomena of Rupture and Flow in Solids," *Phil. Trans. R. Soc. Lond. A*, vol. 221, pp. 163–198, 1921.

[23] V. Vitek, "Intrinsic stacking faults in body-centred cubic crystals," *Phil. Mag.*, vol. 18, pp. 773–786, 1968.

[24] G. Kresse and J. Furthmüller, "Efficiency of ab-initio total energy calculations for metals and semiconductors using a plane-wave basis set," *Comput. Mat. Sci.*, vol. 6, pp. 15–50, 1996.

[25] B. Aradi, B. Hourahine, and T. Frauenheim, "DFTB+, a Sparse Matrix-Based Implementation of the DFTB Method," *J. Phys. Chem. A*, vol. 111, pp. 5678–5684, 2007.

[26] D. Vanderbilt, "Soft self-consistent pseudopotentials in a generalized eigenvalue formalism," *Phys. Rev. B*, vol. 41, pp. 7892–7895, Apr 1990.

[27] J. P. Perdew and Y. Wang, "Accurate and simple analytic representation of the electron-gas correlation energy," *Phys. Rev. B*, vol. 45, pp. 13244–13249, Jun 1992.

[28] N. H. Moreira, G. Dolgonos, B. Aradi, A. L. da Rosa, and T. Frauenheim, "Toward an Accurate Density-Functional Tight-Binding Description of Zinc-Containing Compounds," *J. Chem. Theory Comput.*, vol. 5, pp. 605–614, 2009.

[29] B. Lukose, B. Supronowicz, P. S. Petkov, J. Frenzel, A. B. Kuc, G. Seifert, G. N. Vayssilov, and T. Heine, "Structural properties of metal-organic frameworks within the density-functional based tight-binding method," *Phys. Stat. Sol. B*, vol. 249, pp. 335–342, 2012.

[30] M. Elstner, P. Hobza, T. Frauenheim, S. Suhai, and E. Kaxiras, "Hydrogen bonding and stacking interactions of nucleic acid base pairs: A density-functional-theory based treatment," *J. Chem. Phys.*, vol. 114, pp. 5149–5155, 2001.

[31] A. K. Rappe, C. J. Casewit, K. S. Colwell, W. A. Goddard, and W. M. Skiff, "UFF, a full periodic table force field for molecular mechanics and molecular dynamics simulations," *J. Am. Chem. Soc.*, vol. 114, pp. 10024–10035, 1992.

[32] G. E. Dieter, *Mechanical Metallurgy.* McGraw-Hill Book Company, 1988.

[33] D. J. Eaglesham, A. E. White, L. C. Feldman, N. Moriya, and D. C. Jacobson, "Equilibrium Shape of Si," *Phys. Rev. Lett.*, vol. 70, pp. 1643–1646, Mar 1993.

[34] M. J. Mehl, D. A. Papaconstantopoulos, N. Kioussis, and M. Herbranson, "Tight-binding study of stacking fault energies and the Rice criterion of ductility in the FCC metals," *Phys. Rev. B*, vol. 61, pp. 4894–4897, 2000.

[35] A. P. Côté, A. I. Benin, N. W. Ockwig, M. O'Keeffe, A. J. Matzger, and O. M. Yaghi, "Porous, Crystalline, Covalent Organic Frameworks," *Science*, vol. 310, pp. 1166–1170, 2005.

[36] U. V. Waghmare, E. Kaxiras, V. V. Bulatov, and M. S. Duesbery, "Effects of alloying on the ductility of $MoSi_2$ single crystals from first-principles calculations," *Modelling Simul. Mater. Sci. Eng.*, vol. 6, pp. 493–506, 1998.

[37] T. D. Bennett, A. L. Goodwin, M. T. Dove, D. A. Keen, M. G. Tucker, E. R. Barney, A. K. Soper, E. G. Bithell, J.-C. Tan, and A. K. Cheetham, "Structure and Properties of an Amorphous Metal-Organic Framework," *Phys. Rev. Lett.*, vol. 104, p. 115503, 2010.

[38] J. T. Hughes, T. D. Bennett, A. K. Cheetham, and A. Navrotsky, "Thermochemistry of Zeolitic Imidazolate Frameworks of Varying Porosity," *J. Am. Chem. Soc.*, vol. 135, pp. 598–601, 2013.

[39] H. Zeng, G. Duan, Y. Li, S. Yang, X. Xu, and W. Cai, "Blue Luminescence of ZnO Nanoparticles Based on Non-Equilibrium Processes: Defect Origins and Emission Controls," *Advanced Functional Materials*, vol. 20, no. 4, pp. 561–572, 2010.

[40] V. A. Coleman and C. Jagadish, *Zinc Oxide Bulk, Thin Films and Nanostructures*. Elsevier Ltd., 2006.

[41] J. M. Soler, E. Artacho, J. D. Gale, A. Garca, J. Junquera, P. Ordejn, and D. Snchez-Portal, "The SIESTA method for ab initio order-N materials simulation," *Journal of Physics: Condensed Matter*, vol. 14, no. 11, p. 2745, 2002.

[42] P. Giannozzi, S. Baroni, N. Bonini, M. Calandra, R. Car, C. Cavazzoni, D. Ceresoli, G. L. Chiarotti, M. Cococcioni, I. Dabo, A. D. Corso, S. de Gironcoli, S. Fabris, G. Fratesi, R. Gebauer, U. Gerstmann, C. Gougoussis, A. Kokalj, M. Lazzeri, L. Martin-Samos, N. Marzari, F. Mauri, R. Mazzarello, S. Paolini, A. Pasquarello, L. Paulatto, C. Sbraccia, S. Scandolo, G. Sclauzero, A. P. Seitsonen, A. Smogunov, P. Umari, and R. M. Wentzcovitch, "QUANTUM ESPRESSO: a modular and open-source software project for quantum simulations of materials," *Journal of Physics: Condensed Matter*, vol. 21, no. 39, p. 395502, 2009.

[43] X. Gonze, J.-M. Beuken, R. Caracas, F. Detraux, M. Fuchs, G.-M. Rignanese, L. Sindic, M. Verstraete, G. Zerah, F. Jollet, M. Torrent, A. Roy, M. Mikami, P. Ghosez, J.-Y. Raty, and D. Allan, "First-principles computation of material properties: the {ABINIT} software project," *Computational Materials Science*, vol. 25, no. 3, pp. 478 – 492, 2002.

[44] L. Hedin, "New Method for Calculating the One-Particle Green's Function with Application to the Electron-Gas Problem," *Phys. Rev.*, vol. 139, pp. A796–A823, Aug 1965.

[45] N. Troullier and J. L. Martins, "Efficient pseudopotentials for plane-wave calculations," *Phys. Rev. B*, vol. 43, pp. 1993–2006, Jan 1991.

[46] D. M. Ceperley and B. J. Alder, "Ground State of the Electron Gas by a Stochastic Method," *Phys. Rev. Lett.*, vol. 45, pp. 566–569, Aug 1980.

[47] R. Grau-Crespo, S. Hamad, C. R. A. Catlow, and N. H. de Leeuw, "Symmetry-adapted configurational modelling of fractional site occupancy in solids," *Journal of Physics: Condensed Matter*, vol. 19, no. 25, p. 256201, 2007.

[48] N. A. Hill and U. Waghmare, "First-principles study of strain-electronic interplay in ZnO: Stress and temperature dependence of the piezoelectric constants," *Phys. Rev. B*, vol. 62, pp. 8802–8810, Oct 2000.

[49] P. Schröer, P. Krüger, and J. Pollmann, "First-principles calculation of the electronic structure of the wurtzite semiconductors ZnO and ZnS," *Phys. Rev. B*, vol. 47, pp. 6971–6980, Mar 1993.

[50] M. Usuda, N. Hamada, T. Kotani, and M. van Schilfgaarde, "All-electron GW calculation based on the LAPW method: Application to wurtzite ZnO," *Phys. Rev. B*, vol. 66, p. 125101, Sep 2002.

[51] K. V. K. Rao, S. V. N. Naidu, and L. Iyengar, "Thermal Expansion of Rutile and Anatase," *Journal of the American Ceramic Society*, vol. 53, no. 3, pp. 124–126, 1970.

[52] J. P. Perdew and A. Zunger, "Self-interaction correction to density-functional approximations for many-electron systems," *Phys. Rev. B*, vol. 23, pp. 5048–5079, May 1981.

[53] J. Heyd, G. E. Scuseria, and M. Ernzerhof, "Hybrid functionals based on a screened Coulomb potential," *The Journal of Chemical Physics*, vol. 118, no. 18, pp. 8207–8215, 2003.

[54] M. Mikami, S. Nakamura, O. Kitao, H. Arakawa, and X. Gonze, "First-principles Study of Titanium Dioxide: Rutile and Anatase," *Japanese Journal of Applied Physics*, vol. 39, pp. L847–L850, 2000.

[55] S.-D. Mo and W. Y. Ching, "Electronic and optical properties of three phases of titanium dioxide: Rutile, anatase, and brookite," *Phys. Rev. B*, vol. 51, pp. 13023–13032, May 1995.

[56] X. Gonze and C. Lee, "Dynamical matrices, Born effective charges, dielectric permittivity tensors, and interatomic force constants from density-functional perturbation theory," *Phys. Rev. B*, vol. 55, pp. 10355–10368, Apr 1997.

[57] P. Ghosez, J.-P. Michenaud, and X. Gonze, "Dynamical atomic charges: The case of ABO_3 compounds," *Phys. Rev. B*, vol. 58, pp. 6224–6240, Sep 1998.

[58] A. Vittadini, A. Selloni, F. P. Rotzinger, and M. Grätzel, "Structure and Energetics of Water Adsorbed at tio_2 Anatase 101 and 001 Surfaces," *Phys. Rev. Lett.*, vol. 81, pp. 2954–2957, Oct 1998.